



Research Article

MHD boundary layer micropolar fluid flow over a stretching wedge surface: Thermophoresis and brownian motion effect

Umme HANI¹, Mohammad ALI^{1,*}, Mohammad Shah ALAM¹

¹Department of Mathematics, Chittagong University of Engineering & Technology, Chittagong, 4349, Bangladesh

ARTICLE INFO

Article history

Received: 01 October 2022

Revised: 05 February 2023

Accepted: 08 February 2023

Keywords:

Chemical Reaction; Micropolar Fluid; Micro-rotation; MHD; Radiation; Shooting Method; Stretching Wedge Surface

ABSTRACT

To investigate the consequence of thermophoresis and Brownian diffusion on convective boundary layer micropolar fluid flow over a stretching wedge-shaped surface. The effects of non-dimensional parameters namely coupling constant parameter ($0.01 \leq B_1 \leq 0.05$), magnetic parameter ($1.0 \leq M \leq 15.0$), Grashof number ($0.3 \leq Gr \leq 0.9$), modified Grashof number ($0.3 \leq Gm \leq 0.8$), micropolar parameter ($2.0 \leq G_2 \leq 7.5$), vortex viscosity constraint ($0.02 \leq G_1 \leq 0.2$), Prandtl number ($7.0 \leq Pr \leq 15.0$), thermal radiation parameter ($0.25 \leq R \leq 0.50$), Brownian motion parameter ($0.2 \leq Nb \leq 0.62$), thermophoresis parameter ($0.04 \leq Nt \leq 0.10$), heat generation parameter ($0.1 \leq Q \leq 0.5$), Biot number ($0.65 \leq Bi \leq 1.0$), stretching parameter ($0.2 \leq A \leq 0.5$), Lewis number ($3.0 \leq Le \leq 7.0$), and chemical reaction parameter ($0.2 \leq K \leq 0.7$) on the steady MHD heat and mass transfer is investigated in the present study. The coupled non-linear partial differential equations are reduced into a set of non-linear ordinary differential equations employing similarity transformation. Furthermore, by using the Runge-Kutta method followed by the shooting technique, the transformed equations are solved. The main goal of this study is to investigate the numerical analysis of nanofluid flow within the boundary layer region with the effects of the microrotation parameter and velocity ratio parameter. The novelty of this paper is to propose a numerical method for solving third-order ordinary differential equations that include both linear and nonlinear terms. To understand the physical significance of this work, numerical analyses and tabular displays of the skin friction coefficient, Nusselt number, and Sherwood number are shown. The new approach of the present study contributes significantly to the understanding of numerical solutions to nonlinear differential equations in fluid mechanics and micropolar fluid flow. Micropolar fluids are becoming even more of a focus due to the desire for engineering applications in various fields of medical, mechanical engineering, and chemical processing.

Cite this article as: Hani U, Ali M, Alam MS. MHD boundary layer micropolar fluid flow over a stretching wedge surface: Thermophoresis and brownian motion effect. J Ther Eng 2024;10(2):330–349.

*Corresponding author.

*E-mail address: ali.mehidi93@gmail.com

This paper was recommended for publication in revised form by Editor-in-Chief Ahmet Selim Dalkılıç



INTRODUCTION

The micropolar fluid attracted a great deal of interest from the researcher due to its importance in various fluid fields. The micropolar fluid is the sub-class of micro fluids that exhibits the effects and inertia of micro-rotation. Couple stress and body couples are supported by the micropolar fluids. The bar-like elements containing fluids can effectively symbolize the micropolar fluids. Micropolar fluid is a type of anisotropic fluid like liquid crystals composed of dumbbell molecules. Animal blood is also this type of fluid. Eringen [1] has introduced a fluid model which demonstrates several microscopic effects that arise from the micro-motion as well as the local formation of fluid constituents. The fluids which are consisting of inflexible, indiscriminately oriented, or spherical species suspended in the viscous medium are symbolized by the micropolar fluid model and have ignored the particles' deformation. "Micropolar fluids have been shown to accurately simulate the flow characteristics of polymeric additives, geo-morphological sediments, colloidal suspensions, hematological suspensions, liquid crystals, lubricants, etc." [2]. Various authors have investigated heat and mass transfer boundary layer flow considering micropolar fluid in different physical situations. Srinivasacharya et al. [3] studied the boundary layer free convective flow considering variable wall temperature as well as a concentration in stratified micropolar fluid on a vertical plate. It was noticed that when stratification is present, the sign of microrotation changes within the boundary layer region from negative to positive values. Khalid et al. [4] have investigated natural convection heat and mass transfer boundary layer flow in a micropolar fluid. For this, they have considered the unsteady flow over an infinite oscillating vertical plate and found that the velocity of Newtonian fluid is larger than the velocity of the micropolar fluid. Many researchers have a great interest in the study of nanofluids because of their several applications in different fields like automotive, electronics, computing technology, communications, optical devices, material processing, lasers, medicine, and material amalgamation, etc., while heat dissipation is required. In 1995, Choi and Eastman [5] first invented the nanofluids notion and they have observed high thermal conductivities demonstrated by nanofluids owing to the existence of solid particles which are nanometer (nm) sized. Some authors [6-12] have studied mixed convective heat and mass transfer considering different types of nanofluids with diverse conditions as well as their various applications such as Jilte et al. [13] have tested heat sink cooling concert and focused on the geometry of four channels liquid-cooled heat sink configured in an alternate flow passage concentric shape as well as found that the sink of nanofluid cooled heat compared with water rejected a higher heat rate, on the other hand, Jilte et al. [14] have presented two systems of organizing cooling component which is liquid circulated battery cooling systems (LcBS) and liquid-filled battery cooling systems

(LfBS) containing water-based nanofluid (Alumina 40nm diameter nanoparticles) and the results showed that the production and implementation of Li-ion batteries are easier in electric vehicles for the modular nature of both battery cooling system and LfBS uncomplicated in operation. While the turbulent effect is ignorable, the thermophoresis, as well as Brownian diffusion, play an important role in the fluid flow and Buongiorno [15] has recommended a model considering the consequence of thermophoresis and Brownian diffusion and found that an essential decline of viscosity for a heated fluid in the boundary layer which enhanced heat transfer. A few researchers [16-18] investigated the convective boundary layer flow in diverse fields employing the Buongiorno model.

Due to its use in a variety of sectors, including MHD power generators, plasma studies, nuclear reactor cooling, the petroleum industry, crystal development, and boundary layer control in aerodynamics, magnetohydrodynamics (MHD) plays a significant role in the study of free convection flow. Pavlov [19] has investigated the MHD boundary layer flow over a stretching surface. In his study, he considered a uniform magnetic field and obtained exact similarity solutions. The viscoelastic fluid flow past a stretching surface has been investigated considering a transverse magnetic field [20]. In this regard, he has obtained a set of the exact solution and found that a transverse magnetic field has a similar effect as the viscoelasticity on the fluid flow. On the other hand, Kasiviswanathan and Gandhi [21] have determined a set of the exact solution for the flow of micropolar fluid between infinite non-coaxial revolving disks in the presence of magnetic field effect and observed that the velocity profile is deformed as well as the magnitude of micro-rotation components vector is diminished for the enhance in Hartmann number. Chamkha et al. [22] have investigated the MHD dominated Cu-water nanofluid flow in a porous enclosure and found that for all values of heat generation parameter inside the porous cavity the entropy generation is decreasing for increasing the nanoparticles volume fraction and miniature volume fraction of nanofluid has a significant consequence on the thermal rendering. The Falkner-Skan equation (F-SE) plays a substantial role in the augmentation of fluid dynamics. "The Falkner-Skan equation, a third-order ordinary differential equation over a semi-infinite domain was originally developed in 1931 by Falkner and Skan [23] from a similarity analysis on the steady, two-dimensional, boundary-layer flow of an incompressible, viscous fluid over a wedge [24]". Several researchers [25-28] have reviewed flow over a wedge. The flow with a triangular shape is called a wedge flow. In the procedure under consideration, it can be utilized to pull up one object while keeping another in a plane. The wedge transforms the lateral force into a crosswise splitting force. Later, several authors [29-31] investigated the analytical and numerical solutions of the flow past a wedge considering different flow properties. In high-temperature operating systems radiation has a great impact on the heat and mass

transfer of the fluid flows. Many processes are carried out at a high temperature in the fluid of engineering. In such circumstances, the investigation of radiative heat transfer plays a vital role in the choice of suitable equipment. There aren't many industries that produce gas turbines, radioactive and nuclear power plants, manmade satellites, aircraft, weapons, wind turbines, and other things. Dogonchi et al. [32] have investigated the consequence of radiation and heat source on the heat transfer of nanofluid flow and found significant effects of nanofluid volume fraction and radiation parameter on the Nusselt number. Zheng et al. [33] have found a significant consequence of radiation parameters on the heat transfer of nanofluid flow in their investigation. Ahmed et al. [34] have investigated MHD mixed convection water-based micropolar nanofluids flow in trapezoidal areas numerically and found that average Nusselt number enhances for decreasing values of Richardson number as well as dimensionless viscosity, heat source location, Hartmann number have an essential consequence on the average Nusselt number. Bagh et al. [35] have studied the g-jitter effects on mixed convection for the two colloidal liquids flow which are the alone micropolar nanofluid such as copper/water and micropolar hybrid nanofluid such as alumina-copper/water and observed the distinguished increased performance of hybrid nanofluids in the upper space of inclined sheet g-jitter influenced flow. They also found that the variation of skin friction coefficient and heat flux gradient enhanced with larger values of inflection amplitude. Kasmani et al. [36] investigated the double-diffusive convective boundary layer nanofluid flow past a moving wedge with the effects of Soret and Dufour in the presence of suction and found that the temperature enhances with increasing effect of the Soret parameter as well as declines for the increasing effect of Dufour parameter and the opposite trend arises in case of the mass transfer rate. Ashraf et al. [37] have studied the steady MHD convective tangent hyperbolic nanofluid flows across an elastic

surface with the impact of thermal radiation and thermal conductivity. And they observed that for the increasing effects of the Weissengberg number and power-law index, the velocity profile decreased but the temperature profile increased. Ahmed et al. [38] have identified the consequences of thermal conductivity as well as dynamic viscosity on the boundary layer flow of nanofluid and characteristics of heat transfer over a stretching permeable tube with a heat source/sink. The skin friction coefficient decreases, on the other hand, the local Nusselt number increases for the effects of the Reynolds number and suction/injection parameter. The new approach of the present study contributes significantly to the understanding of numerical solutions to nonlinear differential equations in fluid mechanics and micropolar fluid flow. Micropolar fluids are becoming even more of a focus due to the desire for engineering applications in various fields of medical, mechanical engineering, and chemical processing. This study looks into how thermophoresis and Brownian diffusion affect convective heat and mass transfer boundary layer micropolar fluid flow over a stretching wedge-shaped surface in the presence of thermal radiation and chemical reaction.

MATHEMATICAL MODEL WITH FLOW CONFIGURATION

The two-dimensional steady convective boundary layer flow of viscous, incompressible, and electrically conducting fluid and heat transfer of micropolar fluid over a stretching wedge-shaped surface considering chemical reaction and radiation effects are demonstrated in this study. Coordinate system and configuration of flow as shown in Figure 1. The Cartesian coordinate x - and y -axes are determined along and normal to the surface of the wedge, respectively. Fluid velocities such as u and v act along x - and y - axes, correspondingly. $U_w(x) = ax^m$, where $a > 0$, is the stretching

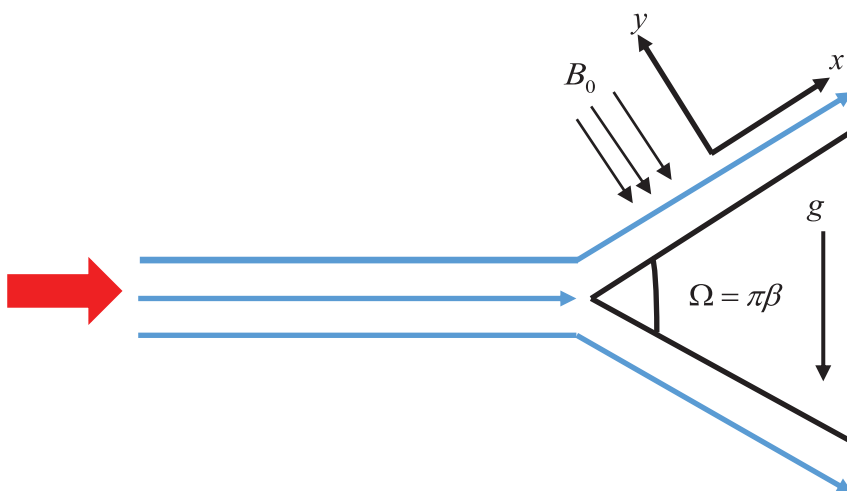


Figure 1. Geometric configuration of wedge flow.

wedge velocity and $U(x) = bx^m$ is the free stream velocity outside the boundary layer of the micropolar fluid. In Figure 1, $\Omega = \pi\beta$ is the wedge angle where β is the Hartree pressure gradient.

Under the above assumptions, the basic equations are considered as [39]:

$$\frac{\partial u}{\partial x} + \frac{\partial v}{\partial y} = 0, \tag{1}$$

$$u \frac{\partial u}{\partial x} + v \frac{\partial u}{\partial y} = U \frac{dU(x)}{dx} + \nu \frac{\partial^2 u}{\partial y^2} + k_1 \frac{\partial N}{\partial y} - \frac{\sigma B_0^2}{\rho_f} (u - U) + \beta_T g (T - T_\infty) + \beta_c^* g (C - C_\infty), \tag{2}$$

$$u \frac{\partial N}{\partial x} + v \frac{\partial N}{\partial y} = -\frac{k}{\rho_j} \left(2N + \frac{\partial u}{\partial y} \right) + \frac{\gamma}{\rho_j} \frac{\partial^2 N}{\partial y^2}, \tag{3}$$

$$u \frac{\partial T}{\partial x} + v \frac{\partial T}{\partial y} = \alpha \frac{\partial^2 T}{\partial y^2} + \tau \left[D_B \frac{\partial C}{\partial y} \frac{\partial T}{\partial y} + \frac{D_T}{T_\infty} \left(\frac{\partial T}{\partial y} \right)^2 \right] - \frac{1}{(\rho C_p)_f} \frac{\partial q_r}{\partial y} + \frac{Q_0}{(\rho C_p)_f} (T - T_\infty), \tag{4}$$

$$u \frac{\partial C}{\partial x} + v \frac{\partial C}{\partial y} = D_B \frac{\partial^2 C}{\partial y^2} + \frac{D_T}{T_\infty} \frac{\partial^2 T}{\partial y^2} - K^* (C - C_\infty). \tag{5}$$

With boundary conditions according to [40]:

$$\text{At } y = 0, \quad u = U_w = ax^m, \quad -k \frac{\partial T}{\partial y} = h_f (T_w - T),$$

$$D_B \frac{\partial C}{\partial y} + \frac{D_T}{T_\infty} \frac{\partial T}{\partial y} = 0, \quad N = -s \left(\frac{\partial u}{\partial y} \right) \text{ and}$$

$$\text{at } y \rightarrow \infty, \quad u \rightarrow U = bx^m, \quad T \rightarrow T_\infty, \quad C \rightarrow C_\infty, \quad N \rightarrow 0.$$

It is to be noted that, “s is a constant such that $0 \leq s \leq 1$. At the wedge surface (i.e. at $y = 0$), $N = 0$, while $s = 0$. It represents the flow of concentrated particles in which the microelements closed to the wall surface are unable to rotate. This case is also known as a strong concentration of microelements. The antisymmetric part of the stress tensor will vanish when $s = 0.5$ consequently concentration of microelements becomes weak. Whereas, the case $s = 1$ is used for the modeling of turbulent boundary layer flows [41]”.

Considering Rossel and approximation the radiative heat flux can be written as

$$q_r = -\frac{4\sigma^*}{3k^*} \frac{\partial T^4}{\partial y}, \tag{6}$$

where σ^* is the Stefan-Boltzmann constant as well as k^* the mean absorption coefficient, and T^4 stand for the linear sum of the temperature. Applying Taylor series expansion T^4 can be expanded T_∞ as:

$$T^4 = T_\infty^4 + 4T_\infty^3 (T - T_\infty) + 6T_\infty^2 (T - T_\infty)^2 + \dots \tag{7}$$

The temperature differences are considered very small, so ignoring the higher order terms involving $(T - T_\infty)$, Eq. (7) one can be written as:

$$T^4 = T_\infty^4 + 4T_\infty^3 (T - T_\infty) \tag{8}$$

Inserting Eq. (8) into Eq. (6) one can be obtained

$$q_r = -\frac{16T_\infty^3 \sigma^*}{3k^*} \frac{\partial T}{\partial y} \tag{9}$$

Therefore Eq. (3) can be written in the form

$$u \frac{\partial T}{\partial x} + v \frac{\partial T}{\partial y} = \alpha \frac{\partial^2 T}{\partial y^2} + \tau \left[D_B \frac{\partial C}{\partial y} \frac{\partial T}{\partial y} + \frac{D_T}{T_\infty} \left(\frac{\partial T}{\partial y} \right)^2 \right] + \frac{1}{(\rho C_p)_f} \frac{16T_\infty^3 \sigma^*}{3k^*} \frac{\partial^2 T}{\partial y^2} + \frac{Q_0}{(\rho C_p)_f} (T - T_\infty), \tag{10}$$

To transfer the set of PDEs (Eqs. (2), (3), (5), and (10)) into a set of dimensionless ODEs introduce the following similarity transformations:

$$\Psi = \left(\frac{2Uxv}{1+m} \right)^{1/2} f, \quad \eta = \left[\frac{(1+m)U}{2xv} \right]^{1/2} y, \quad N = \sqrt{\frac{U(1+m)}{2vx}} U_h, \tag{11}$$

$$\theta(\eta) = \frac{T - T_\infty}{T_w - T_\infty} \text{ and } \phi(\eta) = \frac{C - C_\infty}{C_w - C_\infty},$$

where C_w is the concentration at the stretching surface and T_w is convective fluid temperature. Using Eq. (11) in Eqs. (2), (3), (5), and (10), one can be determined the following ODEs:

$$f''' + \beta(1 - f'^2) + ff'' + B_1 h' + M(1 - f') + Gr\theta + Gm\phi = 0, \tag{12}$$

$$G_2 h'' - 2G_1(2h + f'') - \left(\frac{3m-1}{1+m} \right) hf' + h'f, \tag{13}$$

$$\left(1 + \frac{4}{3}R \right) \theta'' + Pr(f\theta' + Nb\theta'\phi' + Nt\theta'^2 + Q\theta) = 0, \tag{14}$$

$$\phi'' + \frac{Nt}{Nb} \theta'' + Sc(f\phi' - K\phi) = 0, \tag{15}$$

with transformed boundary conditions

$$f(0) = 0, f'(0) = A, \theta'(0) = -Bi[1 - \theta(0)], \quad f(\infty) = 0, \\ f''(0) = A, \theta'(0) = -Bi[1 - \theta(0)] \text{ at } \eta = 0 \\ f'(\infty) \rightarrow 1, h(\infty) \rightarrow 0, \theta(\infty) \rightarrow 0, \phi(\infty) \rightarrow 0, \text{ at } \eta \rightarrow \infty.$$

Where, $f(\eta) = f, \theta(\eta) = \theta, \phi(\eta) = \phi$, Hartree pressure gradient, $\beta = \frac{2m}{1+m}$, Coupling constant parameter, $B_1 = \frac{k_1}{\nu}$, magnetic parameter, $M = \frac{2x\sigma B_0^2}{\rho_j U(1+m)}$, Grashof number, $Gr = \frac{\beta_T g(T_w - T_\infty)x}{U^2(1+m)}$, modified Grashof number $Gm = \frac{\beta_c^* g(C_w - C_\infty)x}{U^2(1+m)}$, micropolar parameter, $G_2 = \frac{\gamma}{\rho\nu j}$, vortex viscosity constraint, $G_1 = \frac{kx}{\rho j U}$, Prandtl number, $Pr = \frac{\nu}{\alpha}$, thermal radiation parameter, $R = \frac{4T_\infty^3 \sigma^*}{\kappa k^*}$, Brownian motion parameter, $Nb = \frac{\tau D_B(C_w - C_\infty)}{\nu}$, Thermophoresis parameter, $Nt = \frac{\tau D_T(T_w - T_\infty)}{\nu T_\infty}$, Heat generation parameter, $Q = \frac{2xQ_0}{(\rho C_p)_f U(1+m)}$, Schmidt number, $Sc = Le \times Pr = \frac{\nu}{D_B}$, Biot number, $Bi = \frac{h_f}{k} \sqrt{\frac{2x\nu}{(1+m)U}}$, stretching parameter, $A = \frac{a}{b}$ and chemical reaction parameter, $K = \frac{2K^*x}{U(1+m)}$.

In the case of $A > 0$ and $A < 0$ the wedge moves in the same and opposite directions, respectively. On the other hand, the wedge will be static while $A = 0$ [42]. The skin friction coefficient, Nusselt number, Sherwood number, and couple stress coefficient are the physical quantities of engineering interest. One can be defined as:

$$C_f = \frac{\tau_w}{\frac{1}{2}\rho_f U_w^2}, Nu = \frac{xQ_w}{\kappa(T_w - T_\infty)}, Sh = \frac{xQ_m}{D_B(C_w - C_\infty)}, Cr = \frac{\gamma}{\gamma U_0^3} \left(\frac{\partial N}{\partial y} \right)_{y=0}$$

τ_w, Q_w and Q_m indicate the shear stress, the transfer rate of heat, and mass per unit area of the surface, respectively. The three quantities are defined as

$$\tau_w = -\mu_f \left(\frac{\partial u}{\partial y} \right)_{y=0}, Q_w = -\kappa \left(\frac{\partial T}{\partial y} \right)_{y=0} \text{ and } Q_m = -D_B \left(\frac{\partial C}{\partial y} \right)_{y=0} \quad (16)$$

With the aid of the above equation (Eq. (16)), one can determine the one-dimensional form of C_f, Nu and Sh, C_r which are proportional to $-f''(0), -\theta'(0)$ and $-\phi'(0), -h'(0)$ respectively.

Solution Procedure

It is impossible to find the exact solution of higher-order nonlinear coupled ordinary differential equations (CODEs). Therefore the numerical solution of the CODEs Eqs. (12) - (15) with boundary conditions are obtained

for the diverse values of concerned physical parameters employing the Runge-Kutta fourth-order method by exploiting symbolic software MATLAB. In this regard Eqs. (12) - (15) along with boundary conditions are converted into a set of first-order ODEs and then are situated into the MATLAB numerical software code to find the solutions. Let us consider into account

$$(y_1, y_2, y_3, y_4, y_5, y_6, y_7, y_8, y_9)^T = (f, f', f'', h, h', \theta, \theta', \phi, \phi'), \quad (16)$$

$$y_3' = \beta(y_2^2 - 1) - y_1 y_3 - B_1 y_5 + M(y_2 - 1) - Gr y_6 - Gm y_8, \quad (17)$$

$$y_5' = \frac{1}{G_2} \left[2G_1(2y_4 + y_3) + \frac{3m-1}{1+m} y_2 y_4 - y_5 y_1 \right] \quad (18)$$

$$y_7' = -Pr \left(1 + \frac{4}{3}R \right)^{-1} \left[y_1 y_7 + Nb y_7 y_9 + Nt y_7^2 + Q y_6 \right], \quad (19)$$

$$y_9' = - \left[-\frac{Pr Nt}{Nb} \left(1 + \frac{4}{3}R \right)^{-1} (y_1 y_7 + Nb y_7 y_9 + Nt y_7^2 + Q y_6) + Sc(y_1 y_9 - K y_8) \right] \quad (20)$$

with boundary conditions

$$y_1 = 0, y_2 = A, y_4 = -y_3, y_7 = -Bi[1 - y_6], Nb y_9 + Nt y_7 = 0, \text{ at } \eta = 0 \\ y_2 \rightarrow 1, y_4 \rightarrow 0, y_6 \rightarrow 0, y_8 \rightarrow 0 \text{ at } \eta \rightarrow \infty. \quad (21)$$

The numerical results of velocity (f'), temperature (θ), and nanoparticle volume fraction (ϕ), angular velocity (h) profiles are calculated for diverse values of obtained physical parameters and presented graphically, as well as discussed physical viewpoint.

RESULTS AND DISCUSSION

The Investigations are conducted on the impacts of the relevant physical parameters on the velocity, temperature, and concentration profiles. Equations (11) through (14) are dimensionless coupled nonlinear ordinary differential equations having boundary conditions (Eq.21) that are numerically solved using the fourth-order Runge-Kutta (RK) technique and the shooting approach. This results in the conversion of Eqs. (11) through (14) into nine first-order ordinary differential equations including boundary conditions, described in Section 3. The typical values of the relevant physical parameters (especially the Prandtl number and Grashof number are taken for the water and the cool surfaces, respectively) are taken into consideration for numerical solutions as coupling constant parameter ($0.01 \leq B_1 \leq 0.05$), magnetic parameter ($1.0 \leq M \leq 15.0$), Grashof number ($0.3 \leq Gr \leq 0.9$), modified Grashof number ($0.3 \leq Gm \leq 0.8$), micropolar parameter ($2.0 \leq G_2 \leq 7.5$) vortex viscosity constraint ($0.02 \leq G_1 \leq 0.2$), Prandtl number ($7.0 \leq Pr \leq 15.0$), thermal radiation parameter ($0.25 \leq R \leq 0.50$), Brownian

motion parameter ($0.2 \leq Nb \leq 0.62$), thermophoresis parameter ($0.04 \leq Nt \leq 0.10$), heat generation parameter ($0.1 \leq Q \leq 0.5$), Biot number ($0.65 \leq Bi \leq 1.0$), stretching parameter ($0.2 \leq A \leq 0.5$), Lewis number ($3.0 \leq Le \leq 7.0$), and chemical reaction parameter ($0.2 \leq K \leq 0.7$). In this section, the impacts of the relevant parameters on velocity, temperature, concentration, and angular velocity are discussed in detail.

Effect of the Magnetic Parameter (M)

Figure 2 depicts the velocity (f'), temperature (θ), concentration (ϕ), and angular velocity (h) profiles for the effect of the magnetic parameter (M). For higher values of the magnetic parameter, a substantial resistive force called the Lorentz

force opposes the fluid motion, and as a result, the rate of heat transfer within the boundary layer increases. It indicates that one of the sources of fluid ruggedness and heat transport is symbolized by the magnetic field. Once higher values of M the velocity (concentration) profile enhance in the range $0 < \eta < 2.5$ ($0 < \eta < 1$) depict in Figures 2a and c, respectively, while the temperature (concentration) profile decreases in the range $0 \leq \eta < 2$ ($1 \leq \eta < 2$) for enhancement of M elucidating Figures 2b and c, respectively. Figures 2a and b also show that, due to the influence of the magnetic parameter, the momentum boundary layer is growing and the thermal boundary layer is shrinking. On the other hand, weak Lorentz force (excited for the effect of magnetic field) guides to deprecation in temperature

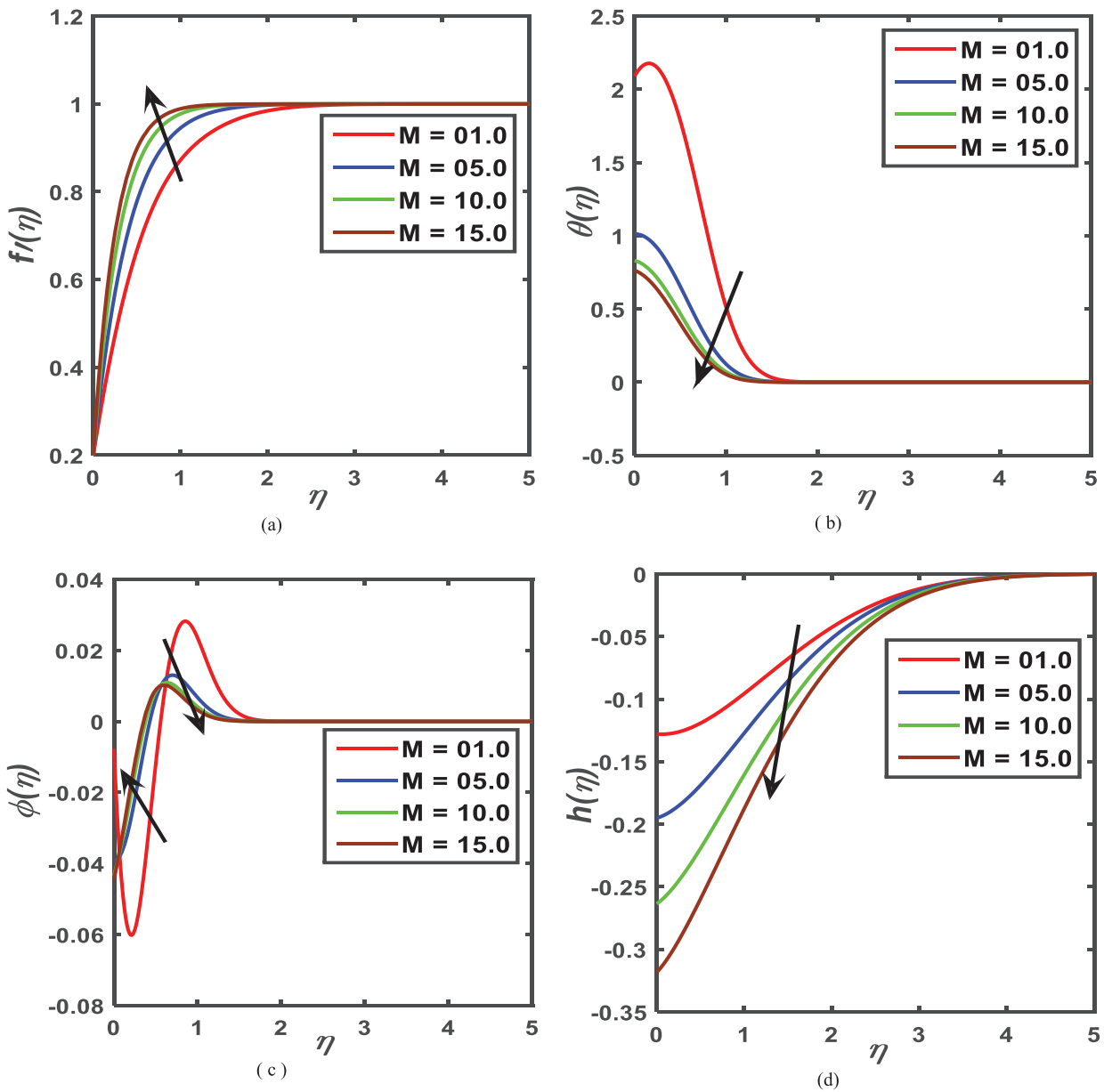


Figure 2. Influence of M on (a) $f'(\eta)$, (b) $\theta(\eta)$, (c) $\phi(\eta)$, and (d) $h(\eta)$ profiles, taking remaining parameters as $m = 0.1$, $Gr = 0.3$, $Gm = 0.3$, $\beta = 0.1$, $Le = 5$, $R = 0.4$, $Pr = 10$, $Nt = 0.1$, $Nb = 0.2$, $Q = 0.5$, $K = 0.5$, $Bi = 1.0$, $A = 0.2$, $B_1 = 0.01$, $G_1 = 0.1$, $G_2 = 2.0$, $s = 0.1$.

and development in velocity profile with prosperous values of the magnetic parameter. Figure 2d elucidates the angular velocity profile (h) for the increasing effect of M . It is seen from the figure that the h is decreasing for increasing values of M in the limit $0 \leq \eta < 4$ and then static.

Effect of Lewis Number (Le)

Figure 3a exhibits the effect of Lewis number (Le) on the velocity profile (f') and found that Le has an inconsequential increasing effect of f' . With increasing values of Le the temperature, the profile is increasing in the range $0 \leq \eta < 1.8$ and then static, which depicts in Figure 3b. Figure 3c

reveals the concentration profile (ϕ) for the effect of Le and it is observed that ϕ is decreasing near the wedge surface ($0 \leq \eta < 1$), but a few distances from the wedge's surface, it is rising in the range $0 \leq \eta < 1.8$ before becoming static due to the improvement of Le . The Lewis number (Le) is the ratio of thermal and mass diffusivities, so while the values of Le enhance, then the rate of thermal diffusion goes ahead to the rate of mass diffusion, and in the fullness of time, the concentration profile declines illustrates in Figure 3c. The effect of Le on the angular velocity profile predicts in Figure 3d and it is seen from the figure that the angular velocity

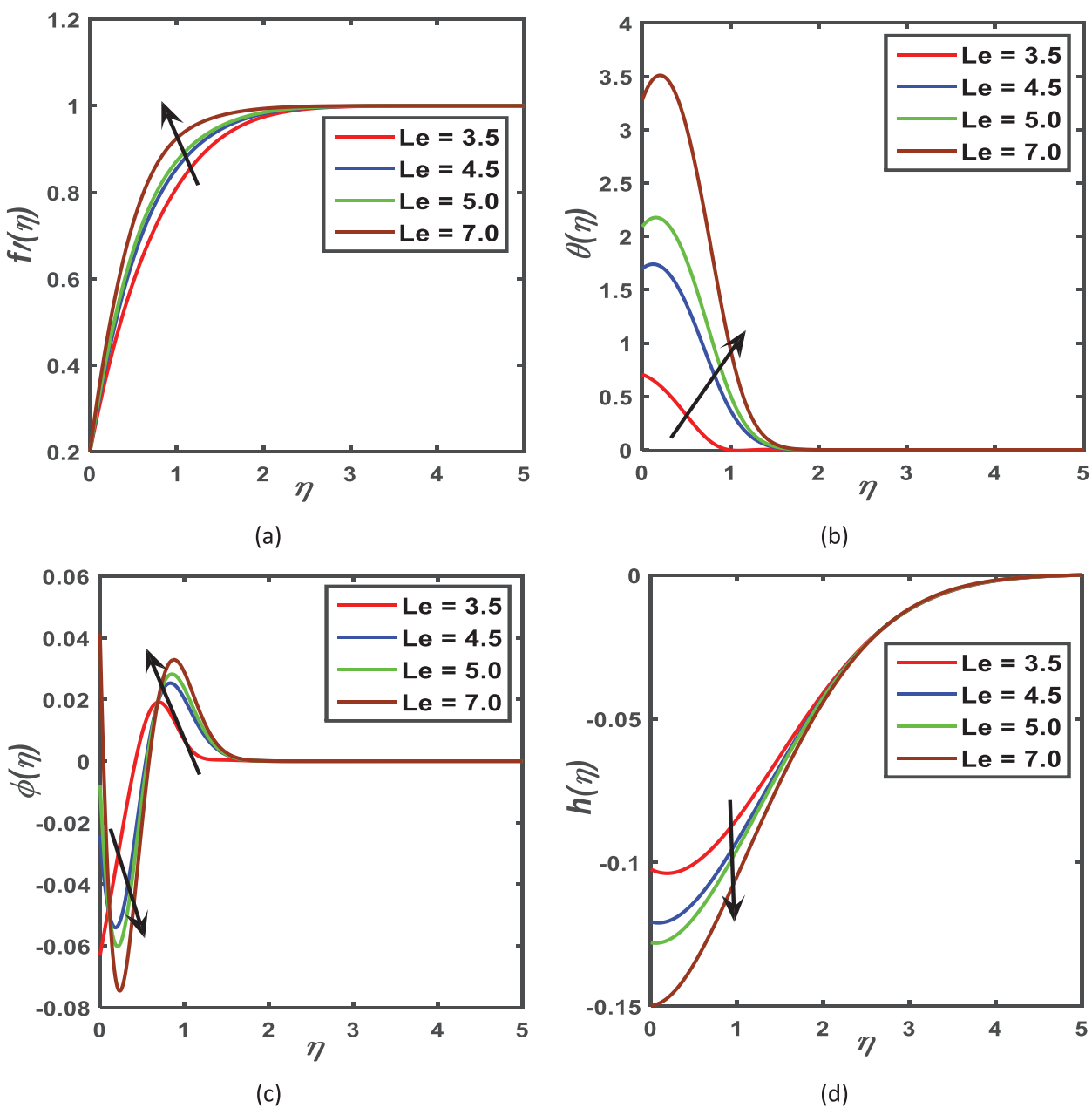


Figure 3. Influence of Le on (a) $f'(\eta)$, (b) $\theta(\eta)$, (c) $\phi(\eta)$, and (d) $h(\eta)$ profiles, taking remaining parameters as $M = 1.0$, $m = 0.1$, $Gr = 0.3$, $Gm = 0.3$, $\beta = 0.1$, $R = 0.4$, $Pr = 10$, $Nt = 0.1$, $Nb = 0.2$, $Q = 0.5$, $K = 0.5$, $Bi = 1.0$, $A = 0.2$, $B_1 = 0.01$, $G_1 = 0.1$, $G_2 = 2.0$, $s = 0.1$.

decreases in the range $1 \leq \eta < 2.4$ and then there is no effect of Le on the angular velocity profile.

Effect of Prandtl Number (Pr)

The impact of the Prandtl number (Pr) on the velocity, temperature, concentration, and angular velocity profiles is depicted in Figures 4a, b, 4c, and d, respectively. Figure 4a demonstrates that the Prandtl number has a slight rising effect on the velocity profile (f') at a small distance from the wedge surface. On the other hand, as the Pr increases, the temperature profile rises close to the wedge surface in the range $0 \leq \eta < 1.5$, and there is no longer an effect, as seen in Figure 4b. This phenomenon physically ascribes as, due

to the larger value of Pr increases the viscous forces of the micropolar fluid with large values of η , consequently the temperature profile increases in the vicinity of the wedge surface. The variation of the concentration profile detects in Figure 4c for the different values Pr and the result indicates that the concentration profile declines close to the wedge surface (in the range $0 \leq \eta < 0.9$) while it is increasing far from the wedge surface ($1 \leq \eta < 2$) and then static with enhance-
sof Pr . These phenomena explain as, for the raising values of the Prandtl number the nanoparticles accumulated into the wedge surface, as a result, the nanoparticle volume fraction profile decrease at the wedge surface and increase far from the wedge surface. The effect of Pr on the angular velocity

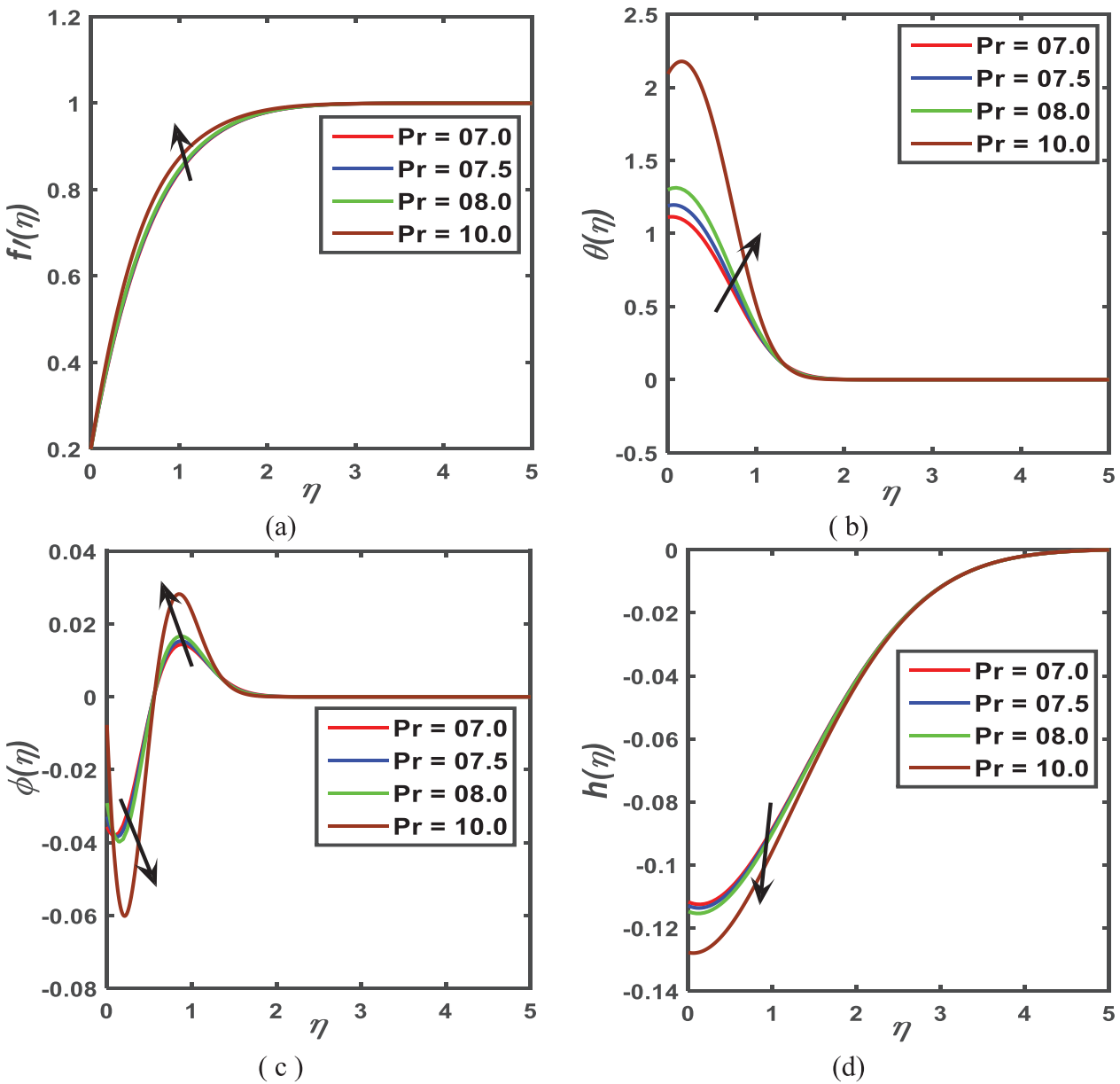


Figure 4. Influence of Pr on (a) $f'(\eta)$, (b) $\theta(\eta)$, (c) $\phi(\eta)$, and (d) $h(\eta)$ profiles, taking remaining parameters as $M = 1.0$, $m = 0.1$, $Gr = 0.3$, $Gm = 0.3$, $\beta = 0.1$, $Le = 5$, $R = 0.4$, $Nt = 0.1$, $Nb = 0.2$, $Q = 0.5$, $K = 0.5$, $Bi = 1.0$, $A = 0.2$, $B_1 = 0.01$, $G_1 = 0.1$, $G_2 = 2.0$, $s = 0.1$.

profile predicts Figure 4d and the graphic illustrates how the angular velocity declines in the range $0 \leq \eta < 2.2$ and then has no further impact on the angular velocity profile.

Effect of Brownian Motion Parameter (Nb)

Figure 5a reveals the effects of the Brownian motion parameter (Nb) on the velocity profile (f') and it is seen that the velocity profile is found to decrease for increasing levels of Nb and progressively increase over η . On the other hand, it is observed from Figure 5b that in the vicinity of the wedge surface, the temperature profile is decreasing for the effect of Nb . It is also observed that for small values of Nb the increasing rate of temperature is perceptible. The

temperature profile of the fluid and the related thermal boundary layer decline because smaller nanoparticles maintain a correlation with higher amounts of Nb . For the effect of Nb , the concentration profile increases in the vicinity of the wedge surface, while it is decreasing far from the wedge surface which is observed in Figure 5c. The motion of the nanoparticles is raised by using higher values of Nb , which causes the concentration profile to grow close to the wedge surface while decreasing farther away. Figure 5d divulges the angular velocity profiles (h) for the increasing effect of Nb . It is seen that the h is increasing for increasing values

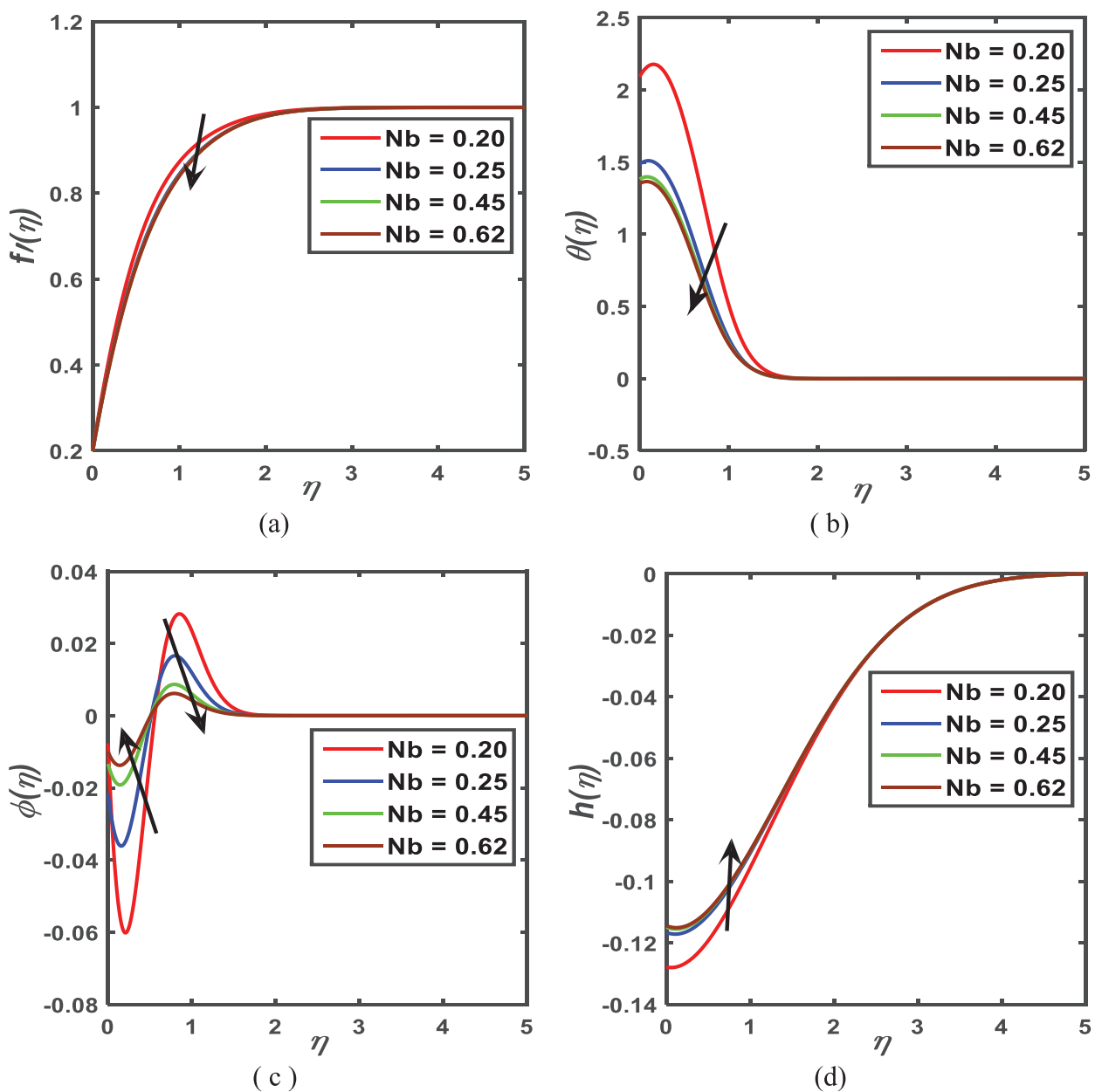


Figure 5. Influence of Nb on (a) $f'(\eta)$, (b) $\theta(\eta)$, (c) $\phi(\eta)$, and (d) $h(\eta)$ profiles, taking remaining parameters as $M = 1.0$, $m = 0.1$, $Gr = 0.3$, $Gm = 0.3$, $\beta = 0.1$, $Le = 5$, $R = 0.4$, $Pr = 10$, $Nt = 0.1$, $Q = 0.5$, $K = 0.5$, $Bi = 1.0$, $A = 0.2$, $B_1 = 0.01$, $G_1 = 0.1$, $G_2 = 2.0$, $s = 0.1$.

of Nb in the limit $0 \leq \eta < 2$ and then there is no effect and finally, it will be static for $\eta > 4$.

Effect of Thermophoresis Parameter (Nt)

Figure 6 demonstrates the velocity, temperature, concentration, and angular velocity profiles for the effect of the thermophoresis parameter, Nt . As can be observed from Figure 6a, the velocity profile is slightly increased by the thermophoresis parameter. The flow steams warm up by thermophoresis, aggravating nanoparticle deprivation in the process. This emphasizes the fluid velocity and speeds up the motion of the nanoparticles. When it comes to the analysis of the temperature and concentration profiles for

nanofluid flow, the thermophoresis parameter is essential. For the consequences of Nt the temperature and concentration profiles are presented in Figures 6b and c, respectively. For the increasing effect of Nt , the temperature profile increases in the vicinity of the surface of the wedge, and away from the wedge surface, the temperature profile becomes static as $\eta \rightarrow \infty$ depicted in Figure 6b. This means that for the effect of the thermophoresis parameter the thermal boundary layer is thicker in the surrounding area of the wedge surface and away from the wedge surface the boundary layer thickness is consistent. Therefore, because of the collision between elevated thermal energy and low-grade energy particles the heat transfer rate increases. From

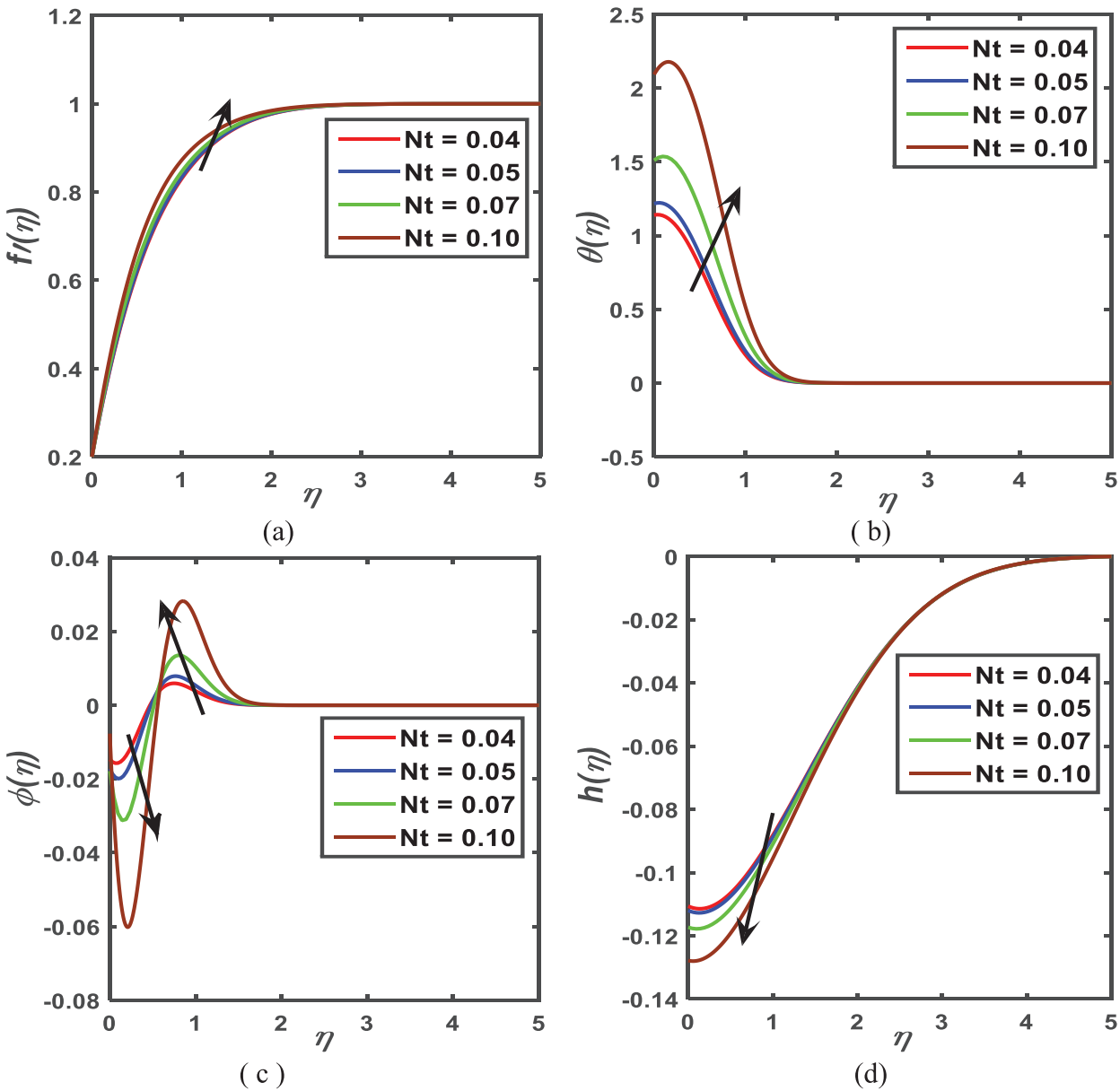


Figure 6. Influence of Nt on (a) $f'(\eta)$, (b) $\theta(\eta)$, (c) $\phi(\eta)$, and (d) $h(\eta)$ profiles, taking the remaining parameter as $M = 1.0$, $m = 0.1$, $Gr = 0.3$, $Gm = 0.3$, $\beta = 0.1$, $Le = 5$, $R = 0.4$, $Pr = 10$, $Nb = 0.2$, $Q = 0.5$, $K = 0.5$, $Bi = 1.0$, $A = 0.2$, $B_1 = 0.01$, $G_1 = 0.1$, $G_2 = 2.0$, $s = 0.1$.

Figure 6c it is found that in the case of the concentration profile, there is a point of intersection and the nanoparticle volume fraction profile is decreasing before the point, the concentration profile increasing after the point for the increasing effect of Nt . Figure 6d elucidates the effect of the thermophoresis parameter, Nt on the angular velocity (h) and found that in the range $0 \leq \eta < 2.5$ the angular velocity decreases with an increase of Nt and there is no effect in the range $\eta > 2.5$, finally, it becomes static in the range $\eta > 4$.

Effect of Biot Number (Bi)

Figure 7a depicts the velocity profile due to the increasing effect of Biot number (Bi) and observed that the velocity profile, as well as momentum boundary thickness,

are increasing. The effect of Bi in the temperature and nanoparticle volume fraction profiles elucidates Figure 7b and c, respectively. From Figure 7b it is seen that the temperature profile is increasing in the range $0 < \eta < 1.75$ with the enhancement of Bi , besides from Figure 7c it is observed that the concentration profile is decreasing in the interval $0 < \eta < 1$ and then increasing in the range $1 \leq \eta < 1.9$ for the increasing effect of Bi . In the range $0 < \eta < 1$, the concentration boundary layer thickness decline, while that of enhanced for the effect of Bi in the range $1 \leq \eta < 1.9$. It is clear that as the Biot number rises, the buoyant force also rises, which causes the fluid's thermal energy to rise more quickly. The increase in fluid density and temperature, as

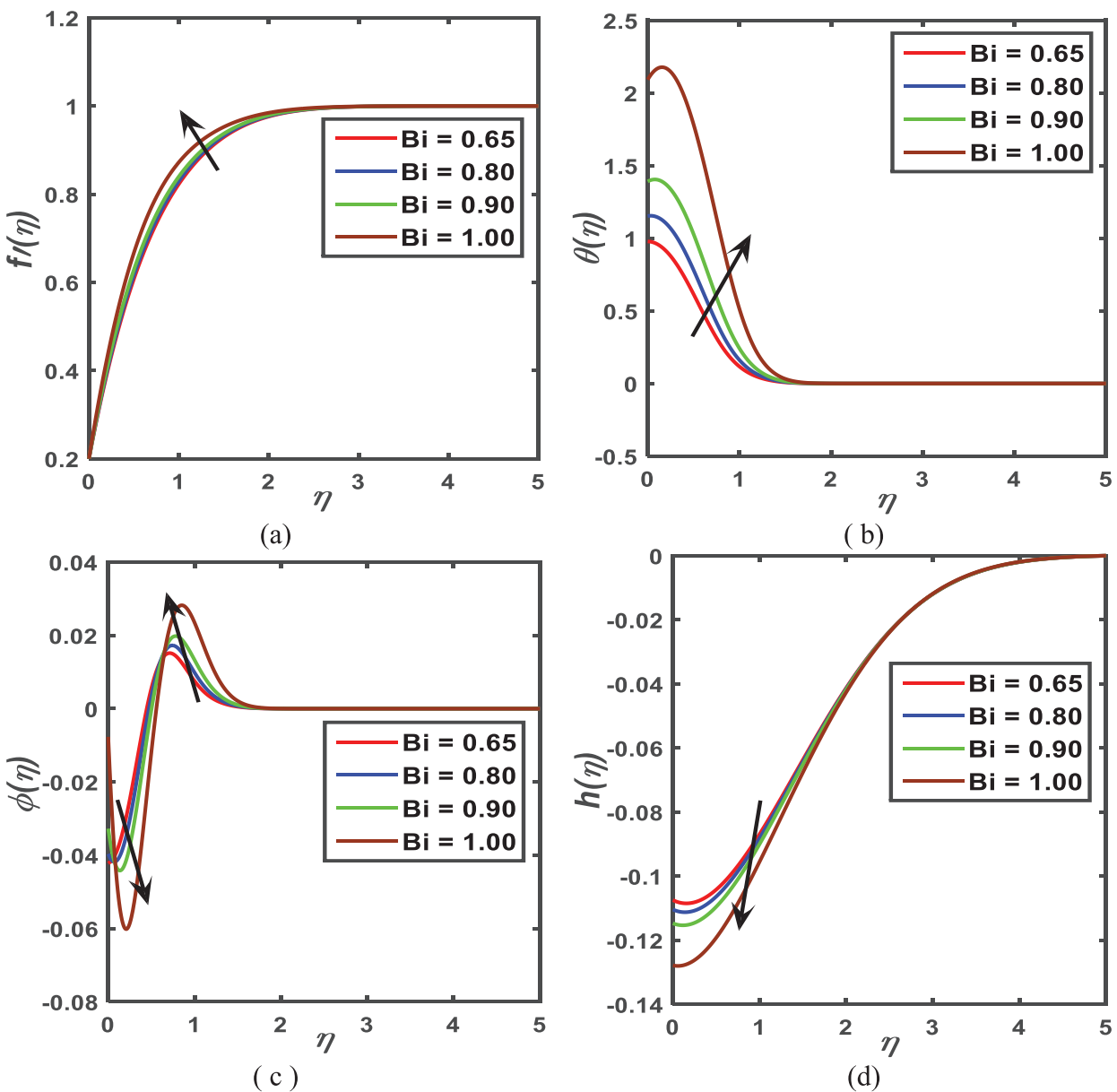


Figure 7. Influence of Bi on (a) $f'(\eta)$, (b) $\theta(\eta)$, (c) $\phi(\eta)$, and (d) $h(\eta)$ profiles, taking remaining parameters as $M = 1.0$, $m = 0.1$, $Gr = 0.3$, $Gm = 0.3$, $\beta = 0.1$, $Le = 5$, $R = 0.4$, $Pr = 10$, $Nt = 0.1$, $Nb = 0.2$, $Q = 0.5$, $K = 0.5$, $A = 0.2$, $B_1 = 0.01$, $G_1 = 0.1$, $G_2 = 2.0$, $s = 0.1$.

well as the enhancement of the fluid's flow by the buoyancy force, are necessary for the thermal energy's extensibility. The Biot number is a measure of how the body's internal conductive resistance compares to its surface-level convective resistance. Therefore, as the Biot number increases, the surface's heat resistance decreases and its temperature rises as a result of enhanced convection. Figure 7d describes the angular velocity (h) for the increasing effect of Bi and found that the h is decreasing in the range $0 \leq \eta < 2.2$, while in the range $2.2 \leq \eta < 4.2$ there is no effect of Bi on h , and then the angular velocity becomes static.

Effect of Chemical Reaction Parameter (K)

Figures 8a and b display the velocity and temperature profiles for the increasing effect of chemical reaction parameter (K) and found that in the vicinity of the surface, the velocity profile decreases in the range $0 < \eta < 2.7$ and then becomes static in the limit $\eta \geq 2.7$, and for the effect of K the temperature profile also decreases in the interval $0 < \eta < 1.7$ and then becomes static. It is also observed that on the surface the temperature profile increases and then gradually decreases with time. Consequently, the momentum, as well as thermal boundary layer thickness, is decreasing

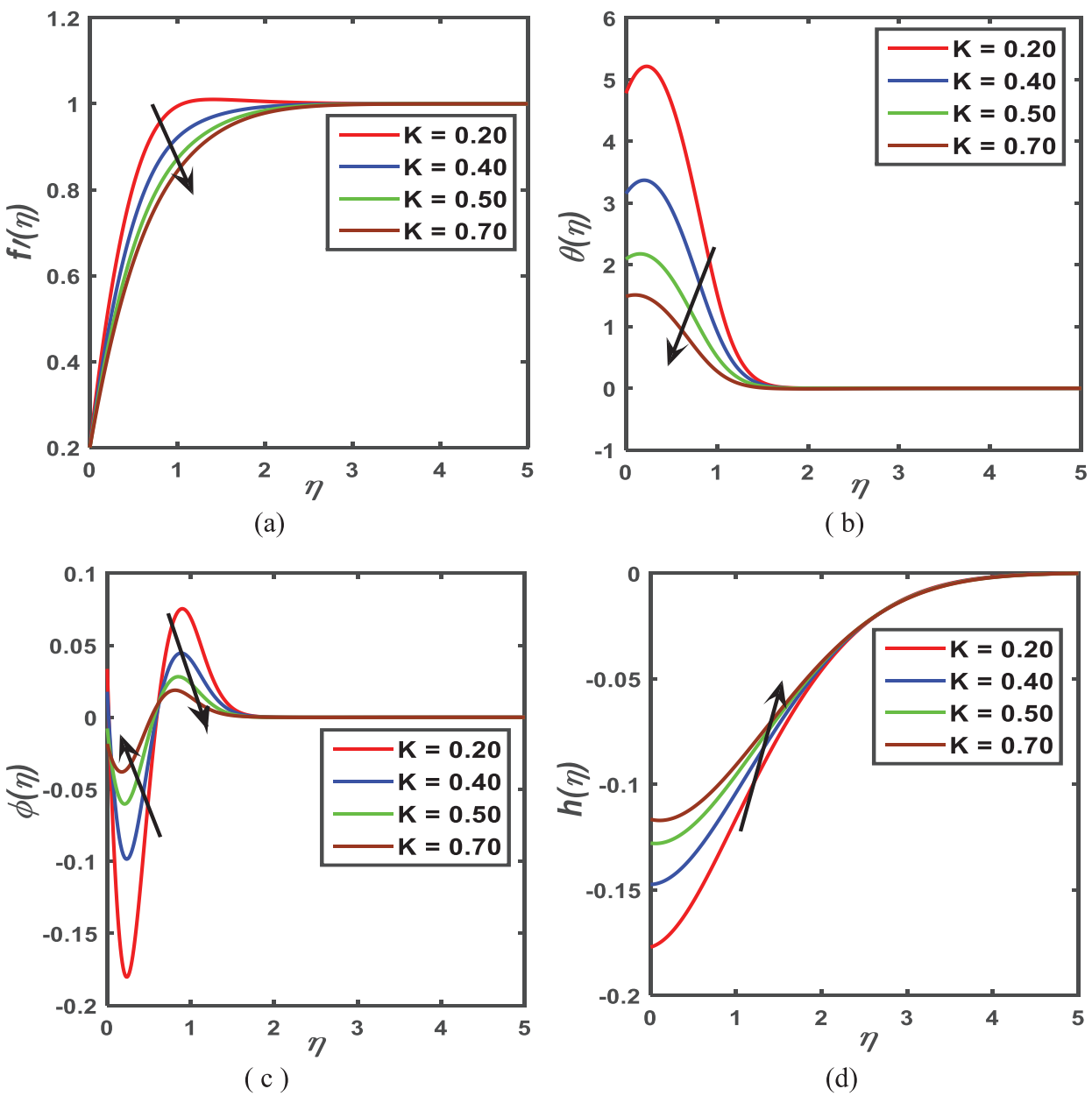


Figure 8. Influence of K on (a) $f'(\eta)$, (b) $\theta(\eta)$, (c) $\phi(\eta)$, and (d) $h(\eta)$ profiles, taking remaining parameters as $M = 1.0$, $m = 0.1$, $Gr = 0.3$, $Gm = 0.3$, $\beta = 0.1$, $Le = 5$, $R = 0.4$, $Pr = 10$, $Nt = 0.1$, $Nb = 0.2$, $Q = 0.5$, $Bi = 1.0$, $A = 0.2$, $B_1 = 0.01$, $G_1 = 0.1$, $G_2 = 2.0$, $s = 0.1$.

with enhances of K . The chemical reaction insertion in the flow scheme is a well-organized method to control the mass and heat transfer. Therefore, the chemical reaction guides the amendment of the flow characteristics. On the other hand, the application of chemical reactions is interconnected with the fields of medicine, manufacturing, and so on. Therefore, the influence of chemical reaction (K) on the concentration profile is displayed in Figure 8c and found that the concentration profile is increasing (decreasing) in the interval $0 \leq \eta < 0.9$ ($0.9 \leq \eta < 1.9$) with the enhancement of K . Consequently, the concentration boundary layer thickness grows up and declines due to the enhancement

of K the neighborhood of the wedge surface and far from the wedge surface, respectively. For the effect of chemical reaction (K) the angular velocity increases in the range $0 \leq \eta < 2.5$ and there is no effect of K on angular velocity in the range $2.5 \leq \eta < 4$, finally, the angular velocity follow the static condition for any η ($\eta \geq 4$) depicts in Figure 8d.

Effect of Radiation Parameter (R)

The effect of radiation parameter (R) on velocity, temperature, concentration, and angular velocity profiles reveal in Figures 9a, b, c, and d, respectively. It is observed from Figure 9a that R has an increasing effect on the velocity profile in the range $0 \leq \eta < 2.2$ and then

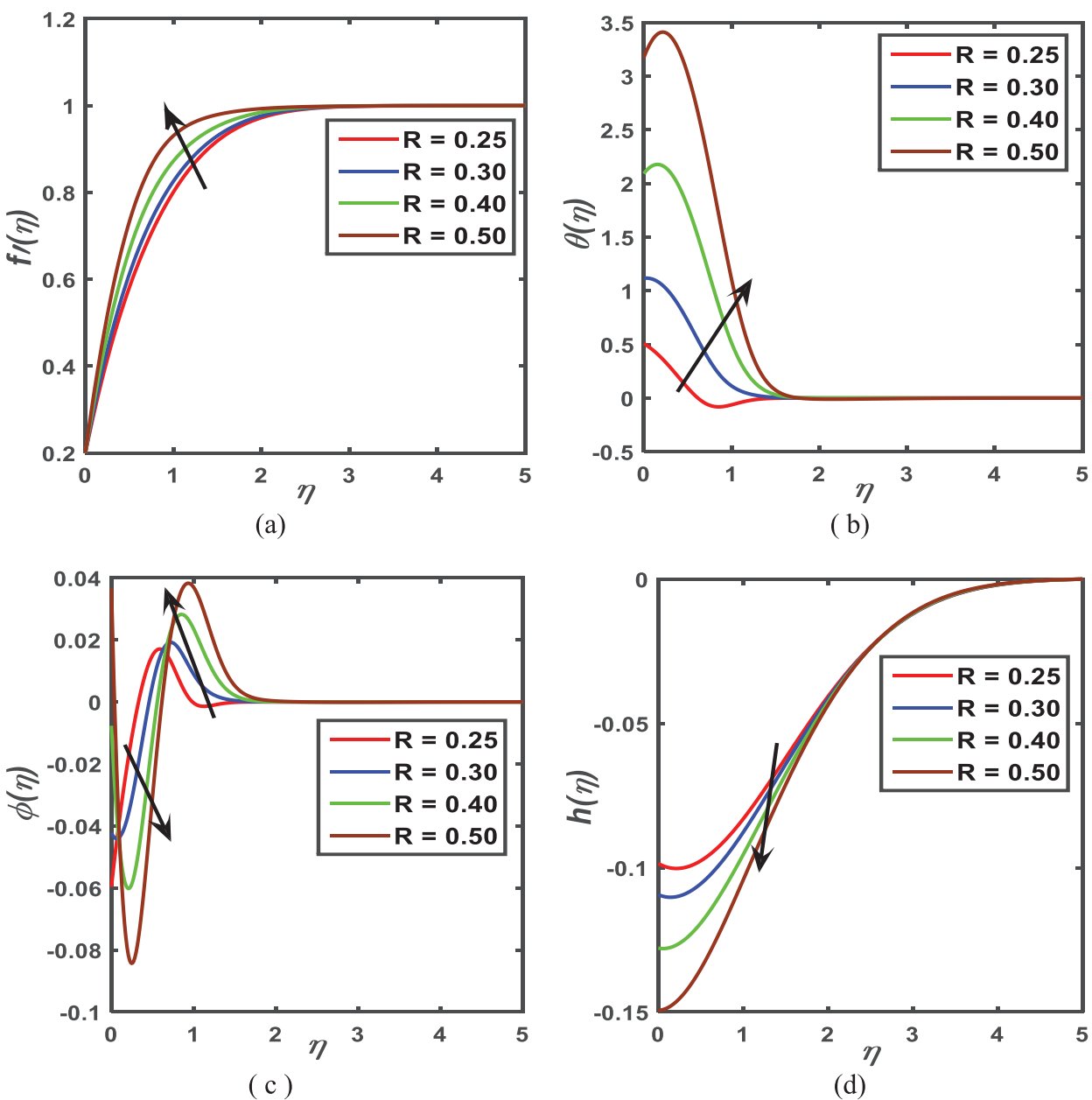


Figure 9. Influence of R on (a) $f'(\eta)$, (b) $\theta(\eta)$, (c) $\phi(\eta)$, and (d) $h(\eta)$ profiles, taking remaining parameters taking as $M = 1.0$, $m = 0.1$, $Gr = 0.3$, $Gm = 0.3$, $\beta = 0.1$, $Le = 5$, $Pr = 10$, $Nt = 0.1$, $Nb = 0.2$, $Q = 0.5$, $K = 0.5$, $Bi = 1.0$, $A = 0.2$, $B_1 = 0.01$, $G_1 = 0.1$, $G_2 = 2.0$, $s = 0.1$.

becomes static. Figures 9b and c expound the temperature and concentration profiles, respectively for the variation of radiation parameters, R . From Figure 9b it is observed that the temperature profile is increasing for the effect of R in the range $0 \leq \eta < 1.8$, consequentl, the thermal boundary layer increases as well. The temperature profile and the thermal boundary layer rise because more energy enters the system due to the increased values of the radiation parameter. It is seen from Figure 9c that there exists a point of intersection and the concentration profile is decreasing before the point and after the point, the nanoparticle volume fraction profile is increasing for enhancement of R . Consequently, the concentration

boundary layer is decreasing as well as increasing for the effect of R in the surrounding area and away from the wedge surface, respectively. In the vicinity of the wedge surface, the angular velocity profile decreases with the increasing effect of R depicted in Figure 9d.

Effect of Vortex Viscosity Constraint (G_1)

Figure 10 demonstrates the velocity, temperature, concentration, and angular velocity profiles for $G_1 = 0.020, 0.065, 0.070,$ and 0.100 , taking the remaining parameters are constant. Figure 11a displays the effect of G_1 on the velocity profile. Velocity profile as well as momentum boundary layer thickness increase in the range $0 \leq \eta < 2.5$ and then follow the static condition for large values of η (η

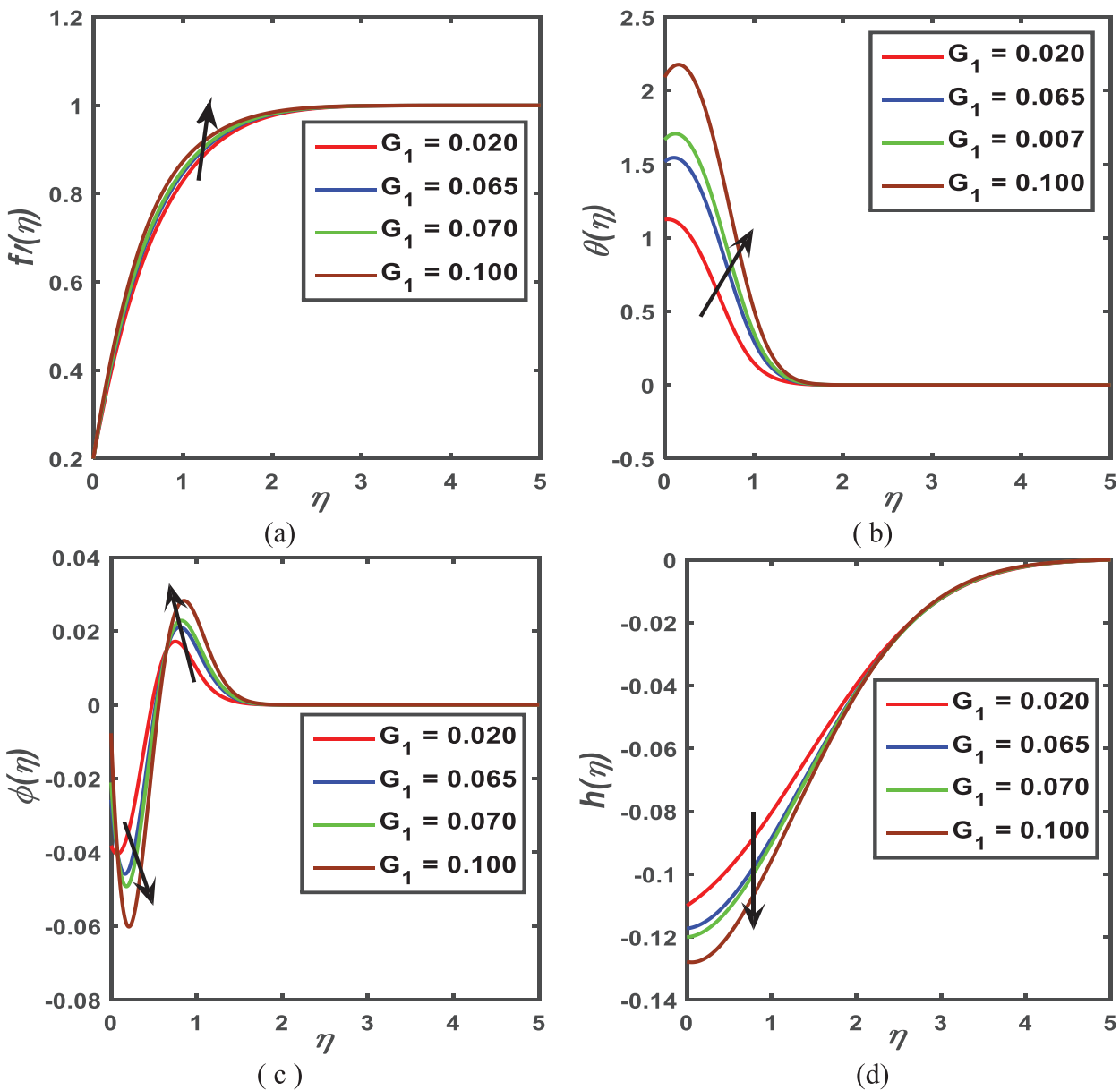


Figure 10. Influence of G_1 on (a) $f'(\eta)$, (b) $\theta(\eta)$, (c) $\phi(\eta)$, and (d) $h(\eta)$ profiles, taking remaining parameters as $M = 1.0, m = 0.1, Gr = 0.3, Gm = 0.3, \beta = 0.1, Le = 5, R = 0.4, Pr = 10, Nt = 0.1, Nb = 0.2, Q = 0.5, K = 0.5, Bi = 1.0, A = 0.2, B_1 = 0.01, G_2 = 2.0, s = 0.1$.

≥ 2.5). In the vicinity of the wedge surface, the temperature (concentration) profiles decrease which reveals Figure 10b (Figure 10c). From Figure 10c, it is observed that being far away from the wedge surface G_1 leads to increasing the concentration profile. Figure 10d exposes the effect of G_1 on the angular velocity profile and found that in the range $0 \leq \eta < 2.2$ the angular velocity profile decreases, and at a certain range $2.2 \leq \eta < 4.2$ there is no effect of G_1 .

Effect of Micropolar Parameter (G_2)

Figure 11a demonstrates the velocity profile $G_2 = 2.0, 2.5, 4.5,$ and 7.5 taking the remaining parameters as

constant. From Figure 11a it is seen that the velocity profile decreases in the range $0 \leq \eta < 2.2$, while it becomes static in the range $\eta \geq 2.2$. Figure 11b displays the effect of G_2 the temperature profile and found that temperature profile as well as thermal boundary layer thickness decrease in the vicinity of the wedge surface ($0 \leq \eta < 1.45$) and then follows the static condition for large values of η ($\eta \geq 1.45$). Near the wedge surface, the concentration profile increases in the range $0 \leq \eta < 1$ revealed in Figure 11c. From Figure 11c, it is observed that being far away from the wedge surface G_2 leads to decreasing the concentration profile in the range $1 \leq \eta < 2$. Figure 11d exposes

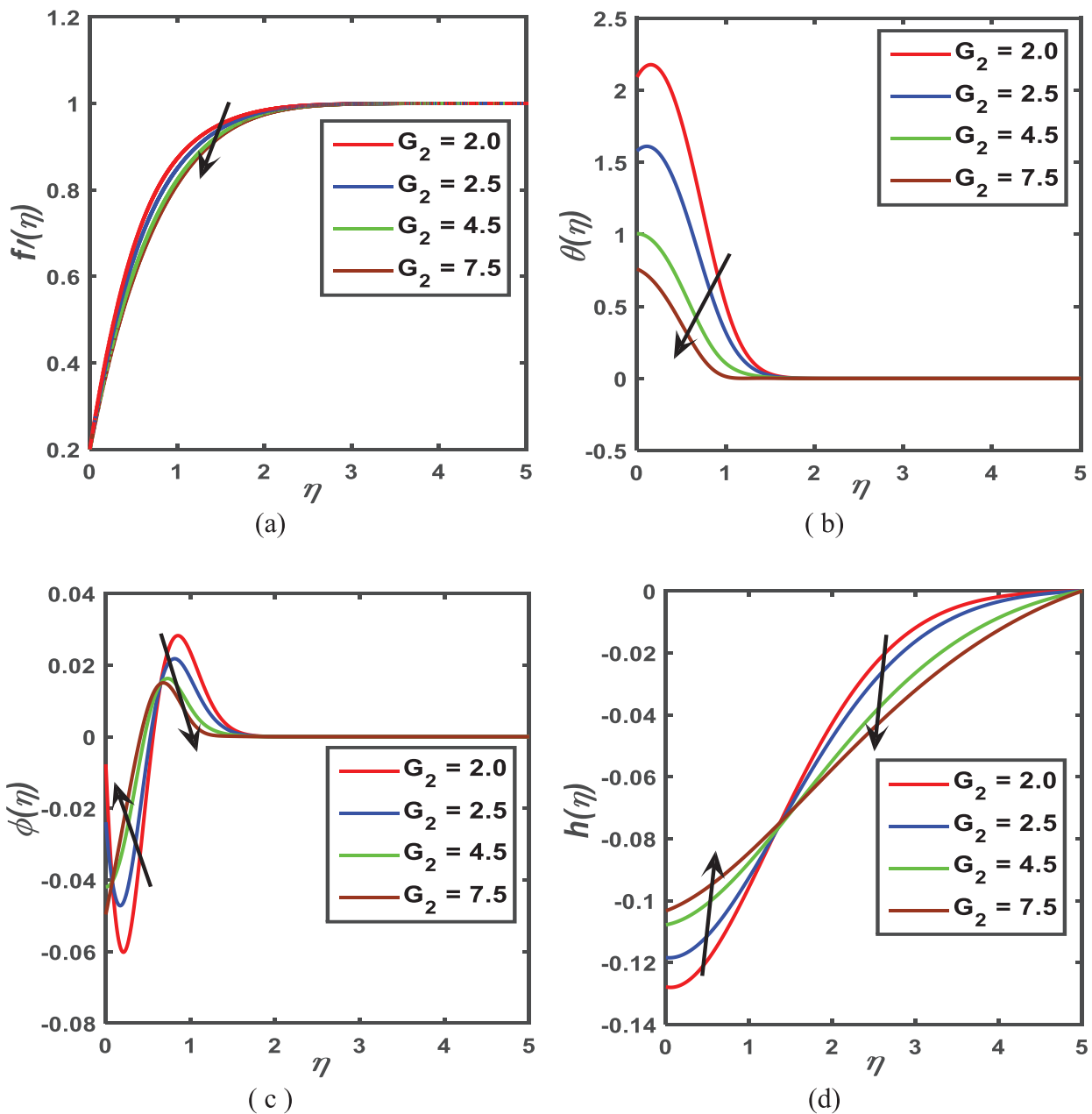


Figure 11. Influence of G_2 on (a) $f'(\eta)$, (b) $\theta(\eta)$, (c) $\phi(\eta)$, and (d) $h(\eta)$ profiles, taking remaining parameters as $M = 1.0, m = 0.1, Gr = 0.3, Gm = 0.3, \beta = 0.1, Le = 5, R = 0.4, Pr = 10, Nt = 0.1, Nb = 0.2, Q = 0.5, K = 0.5, Bi = 1.0, A = 0.2, B_1 = 0.01, G_1 = 0.1, s = 0.1$.

the effect of G_2 on the angular velocity profile and found that in the range $0 \leq \eta < 1.5$ the angular velocity profile increases, and at a certain range $1.5 \leq \eta < 5.0$ the angular velocity decreases for the effect of G_2 .

Effect of Coupling Constant Parameter (B_1)

Figure 12a demonstrates the velocity profile $B_1 = 0.1, 0.2, 0.4$, and 0.5 , taking the remaining parameters as constant. From Figure 12a it is observed that B_1 has an insignificant decreasing effect on the velocity profile in the range $0 \leq \eta < 2.5$, while it becomes static in the range $\eta \geq 2.5$. Figure 12b displays the temperature profile for $B_1 = 0.1, 0.2, 0.4$, and 0.5 and found that temperature profile

as well as thermal boundary layer thickness decrease in the vicinity of wedge surface ($0 \leq \eta < 1.5$) and then follow the static condition for large values of η ($\eta \geq 1.5$). Near the wedge surface, the concentration profile increases in the range $0 \leq \eta < 0.8$ revealed in Figure 12c. From Figure 12c, it is observed that being far away from the wedge surface B_1 leads to decreasing the concentration profile in the range $0.8 \leq \eta < 1.7$. Figure 12d exposes the effect of B_1 on the angular velocity profile and found that in the range $0 \leq \eta < 1.8$ the angular velocity profile increases, and in the range $1.5 \leq \eta < 5.0$ there is no effect of B_1 .

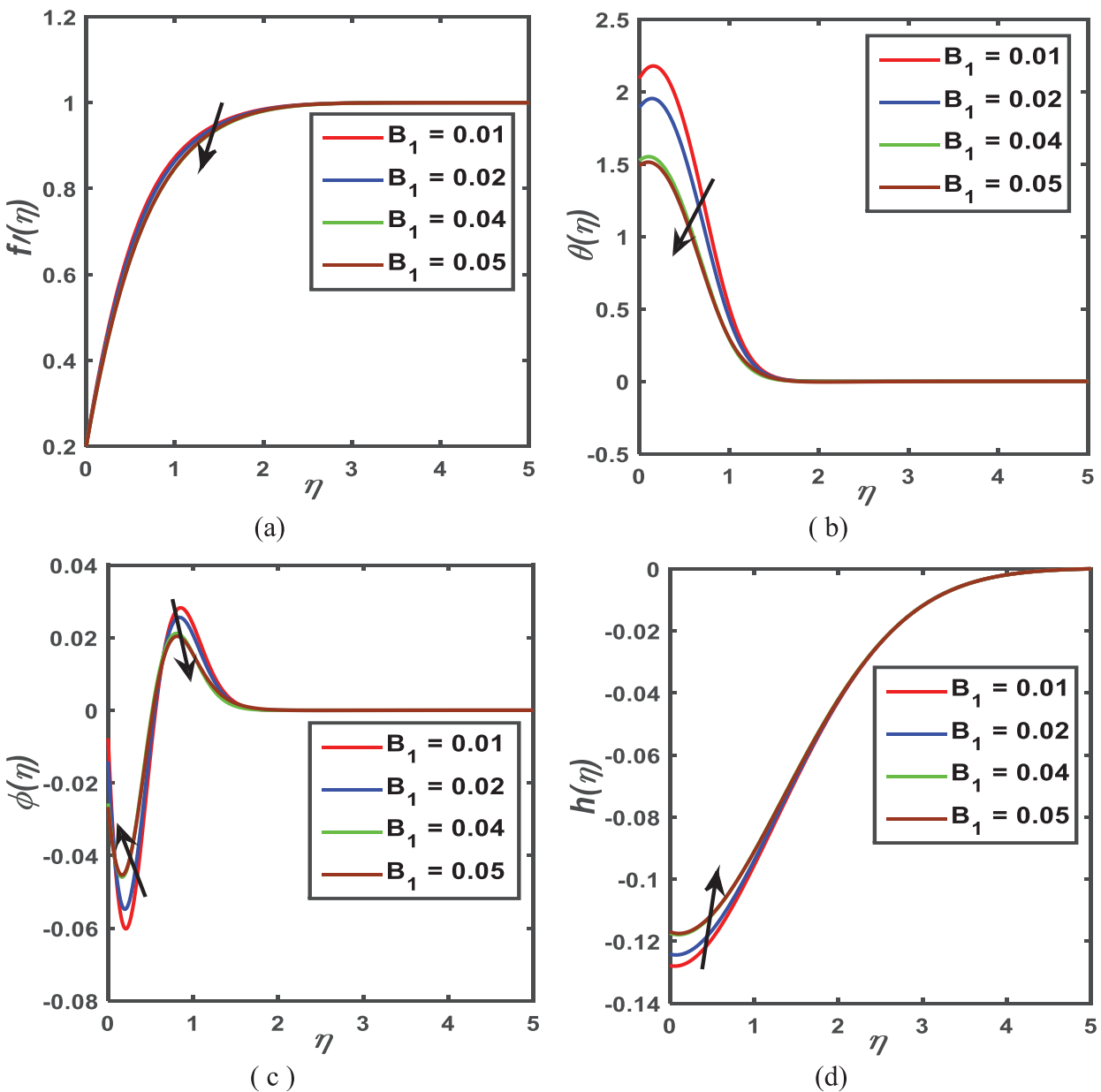


Figure 12. Influence of B_1 on (a) $f'(\eta)$, (b) $\theta(\eta)$, (c) $\phi(\eta)$, and (d) $h(\eta)$ profiles, taking remaining parameters as $M = 1.0$, $m = 0.1$, $Gr = 0.3$, $Gm = 0.3$, $\beta = 0.1$, $Le = 5$, $R = 0.4$, $Pr = 10$, $Nt = 0.1$, $Nb = 0.2$, $Q = 0.5$, $K = 0.5$, $Bi = 1.0$, $A = 0.2$, $G_1 = 0.1$, $G_2 = 2.0$, $s = 0.1$.

Table 1. Skin friction coefficient ($-f''(0)$), Nusselt number ($-\theta'(0)$), Sherwood number ($-\phi'(0)$), and Couple stress coefficient ($-h'(0)$) for distinct values of $M, \beta, Le, Nt, Nb, K,$ and A , taking remaining parameters as: $m = 0.1, Gr = 0.3, Gm = 0.3, R = 0.4, Pr = 10, Q = 0.5, Bi = 1.0, B_1 = 0.01, G_1 = 0.1, G_2 = 2.0,$ and $s = 0.1$.

M	β	Le	Nt	Nb	K	A	$-f''(0)$	$-\theta'(0)$	$-\phi'(0)$	$-h'(0)$
1.0	0.1	5.0	0.1	0.2	0.5	0.2	-1.2784	-1.0919	0.5459	0.0061
5.0	0.1	5.0	0.1	0.2	0.5	0.2	-1.9507	-0.0123	0.0061	-0.0213
10.0	0.1	5.0	0.1	0.2	0.5	0.2	-2.6366	0.1687	-0.0843	-0.0508
15.0	0.1	5.0	0.1	0.2	0.5	0.2	-3.1834	0.2366	-0.1183	-0.0750
1.0	0.3	5.0	0.1	0.2	0.5	0.2	-1.3132	-0.8354	0.4177	0.0275
1.0	0.5	5.0	0.1	0.2	0.5	0.2	-1.3779	-0.7678	0.3839	0.0261
1.0	0.7	5.0	0.1	0.2	0.5	0.2	-1.4117	-0.5348	0.2674	0.0253
1.0	0.1	3.5	0.1	0.2	0.5	0.2	-1.0233	0.2937	-0.1469	0.0153
1.0	0.1	4.5	0.1	0.2	0.5	0.2	-1.2060	-0.6971	0.5459	0.0061
1.0	0.1	7.0	0.1	0.2	0.5	0.2	-1.4972	-2.2759	1.1379	-0.0017
1.0	0.1	5.0	0.04	0.2	0.5	0.2	-1.1064	-0.1393	0.0279	0.0123
1.0	0.1	5.0	0.05	0.2	0.5	0.2	-1.1201	-0.2164	0.0541	0.0118
1.0	0.1	5.0	0.07	0.2	0.5	0.2	-1.1732	-0.5104	0.1786	0.0099
1.0	0.1	5.0	0.1	0.25	0.5	0.2	-1.1663	-0.4855	0.1942	0.0101
1.0	0.1	5.0	0.1	0.45	0.5	0.2	-1.1491	-0.3821	0.0849	0.0107
1.0	0.1	5.0	0.1	0.62	0.5	0.2	-1.1443	-0.3513	0.0567	0.0110
1.0	0.1	5.0	0.1	0.2	0.2	0.2	-1.7712	-3.7799	1.8899	-0.0115
1.0	0.1	5.0	0.1	0.2	0.4	0.2	-1.4741	-2.1529	1.0765	-8.0455
1.0	0.1	5.0	0.1	0.2	0.7	0.2	-1.1657	-0.4875	0.2437	0.0101
1.0	0.1	5.0	0.1	0.2	0.5	0.3	-1.0428	-0.3889	0.1945	0.0081
1.0	0.1	5.0	0.1	0.2	0.5	0.4	-0.8546	0.0454	-0.0227	0.0084
1.0	0.1	5.0	0.1	0.2	0.5	0.5	-0.7121	0.2105	-0.1052	0.0070

Table 2. The correlation coefficient for the mentioned parameters of the skin friction $f''(0)$, the Nusselt number $\theta'(0)$, the Sherwood number $\phi'(0)$, and the couple stress coefficient $h'(0)$ by taking 2nd order coefficient

	M	β	Le	Nt	Nb	K	A	$f''(0)$	$\theta'(0)$	$\phi'(0)$	$h'(0)$
M	1.00										
β	-0.13	1.00									
Le	0.00	0.00	1.00								
Nt	0.14	0.14	0.00	1.00							
Nb	-0.12	-0.12	0.00	0.13	1.00						
K	0.04	0.04	0.00	-0.04	0.04	1.00					
A	-0.13	-0.13	0.00	0.14	-0.12	0.04	1.00				
$f''(0)$	-0.92	0.01	-0.13	-0.19	0.15	0.17	0.38	1.00			
$\theta'(0)$	0.31	-0.01	-0.41	-0.16	0.09	0.68	0.27	0.03	1.00		
$\phi'(0)$	-0.29	0.02	0.38	0.19	-0.16	-0.67	-0.25	-0.04	-0.99	1.00	
$h'(0)$	0.06	0.08	0.00	-0.09	0.07	0.25	0.08	0.04	0.35	-0.35	1.00

Correlation Analysis

From Table 2 it is seen that $\beta, Nb, K,$ and A are positively correlated with a velocity gradient but $M, Le,$ and Nt are negatively correlated with a velocity gradient. Higher values of one variable tend to result in higher values of another

variable whenever there is a positive correlation, but the opposite is true when there is a positive correlation. If the numerical values are 0.25 or above, the correlations between variables are statistically significant. So, from Table 2 it is also observed that the temperature gradient is positively

correlated with M , Nb , and K but negatively correlated with β , Le , Nt , and A respectively. The concentration is positively correlated with β , Le , and Nt but negatively correlated with M , Nb , K and A . Again, the couple stress coefficient is positively correlated with β , Le , M , Nb , K , and A but negatively correlated with Nt .

CONCLUSION

Under consideration of the impact of the concerned physical parameters, a computational examination of the MHD boundary layer of micropolar fluid flow across a stretched wedge is carried out. The Buongiorno model is taken into account for this. The significant findings of this investigation are listed as :

- The magnetic parameter act as a controlling parameter in this study because fluid velocity and the rate of temperature enhance but the rate of mass transfer decreases within the boundary layer region consequence of the magnetic parameter.
- The Brownian motion parameter acts as a source of cooling but the thermophoresis parameter acts as a heat source parameter because, within the boundary layer region, the temperature of the fluid decreases for the effect of the Brownian motion parameter on the other hand the reverse results arises for thermophoresis parameter.
- The stretching or velocity ratio parameters act as a formation of the boundary layer. While the surface velocity is less than the free stream velocity, the structure of the boundary layer will be inverted but the opposite shape is formed when the surface velocity is greater than the free stream velocity. In the study, one can find the reverse inverted shape boundary layer.

NOMENCLATURE

Latin alphabet

C_p	Specific heat at constant pressure [$\text{Jkg}^{-1} \text{K}^{-1}$]
B_0	Strength of transverse magnetic field [$\text{kg s}^{-2} \text{A}^{-1}$]
u	Velocity component of micropolar along x - direction [ms^{-1}]
v	Velocity component of micropolar along y - direction [ms^{-1}]
Ω	Wedge angle
β	The gradient of Hartree pressure [Nm^{-3}]
σ^*	Stefan-Boltzmann constant [$\text{Wm}^{-2}\text{K}^{-4}$]
k^*	Mean absorption coefficient
U_w	The stretching velocity of the surface [ms^{-1}]
U	Free stream velocity of the fluid [ms^{-1}]
$f(\eta)$	Dimensionless stream function
$f'(\eta)$	Dimensionless velocity
$f''(\eta)$	Dimensionless velocity gradient
a	Stretching rate constant
b	The free stream rate constant
Q_0	Heat generation

K^*

Chemical reaction

β_T

Volumetric coefficient of thermal expansion [K^{-1}]

β_c^*

Volumetric coefficient expansion of nanoparticle volume fraction

g

Acceleration due to gravity vector [ms^{-2}]

T

The dimensional temperature of the fluid [K]

T_w

Convective fluid temperature [K]

T_∞

Ambient nanofluid temperature [K]

C

The dimensional nanoparticle volume fraction [kg m^{-3}]

C_w

Nanoparticle volume fraction at the stretching surface [kg m^{-3}]

C_∞

Free stream nanoparticle volume fraction [kg m^{-3}]

D_B

Brownian diffusion coefficient [$\text{cm}^2 \text{s}^{-1}$]

D_T

Thermophoresis diffusion coefficient

q_r

Radiative heat flux [Wm^{-2}]

h_f

Coefficient of heat transfer

k_1

Coupling constant

N

micro-rotation or angular velocity [rads^{-1}]

K

Thermal conductivity [Wm^{-1}K]

j

Microinertia density

Greek alphabet

γ

Spin gradient

τ

The ratio of nanoparticle effective heat capacity and base fluid heat capacity

τ_w

Shear stress [Nm^{-2}]

σ

Electrical conductivity [Sm^{-1}]

ρ

The density of the base fluid [kgm^{-3}]

$(\rho C_p)_f$

Micropolar heat capacity

α

Thermal diffusivity of base fluid [m^2s^{-1}]

ν

Kinematic viscosity of the base fluid [kg m^{-3}]

J

Stream function [m^2s^{-1}]

$\theta(\eta)$

Dimensionless temperature

$\theta'(\eta)$

Rate of temperature

$\phi(\eta)$

The dimensionless nanoparticle volume fraction

$\phi'(\eta)$

Rate of nanoparticle volume fraction

Dimensionless numbers/parameters

M

Magnetic parameter

Gr

Grashof number

Gm

Modified Grashof number

Pr

Prandtl number

R

Thermal radiation parameter

Nb

Brownian motion parameter

Nt

Thermophoresis parameter

Q

Heat generation parameter

Sc

Schmidt number

Bi

Biot number

A

Stretching parameter

Le

Lewis number

K

Chemical reaction parameter

B_1

Coupling constant parameter

G_1

Vortex viscosity constraint

G_2

Micropolar parameter

Q_w	Transfer rate of heat per unit area of the surface
Q_m	Transfer rate of mass per unit area of the surface
C_f	skin friction coefficient
Nu	Nusselt number
Sh	Sherwood number

Abbreviations

BL	Boundary layer
MHD	Magnetohydrodynamic
PDE's	Partial Differential Equations
ODEs	Ordinary Differential Equations
CODEs	Coupled Ordinary Differential Equations
BCs	Boundary conditions

AUTHORSHIP CONTRIBUTIONS

Authors equally contributed to this work.

DATA AVAILABILITY STATEMENT

The authors confirm that the data that supports the findings of this study are available within the article. Raw data that support the finding of this study are available from the corresponding author, upon reasonable request.

CONFLICT OF INTEREST

The author declared no potential conflicts of interest with respect to the research, authorship, and/or publication of this article.

ETHICS

There are no ethical issues with the publication of this manuscript.

REFERENCES

- [1] Eringen AC. Theory of micropolar fluids. *J Math and Mech* 1966;6:1–18. [\[CrossRef\]](#)
- [2] Reddy GVR, Krishna YH. Soret and Dufour effects on MHD micropolar fluid flow over a linearly stretching sheet through a non-darcy porous medium. *Int J Appl Mech Eng* 2018;23:485–502. [\[CrossRef\]](#)
- [3] Srinivasacharya D, Upendra M. Effect of double stratification on MHD free convection in a micropolar fluid. *J Egypt Math Soc* 2013;21:370–378. [\[CrossRef\]](#)
- [4] Khalid A, Khan I, Khan A, Shafie S. Conjugate transfer of heat and mass in the unsteady flow of a micropolar fluid with wall couple stress. *AIP Adv* 2015;5:127125. [\[CrossRef\]](#)
- [5] Choi SUS, Eastman JA. Enhancing thermal conductivity of fluids with nanoparticles, Proc. Int. mech. Eng. congress and exhibition 2015, San Francisco, CA(United States), Nov. 12-17, 1995.
- [6] Mebarek-Oudina F, Chaban I. Review on nano-fluids applications and heat transfer enhancement techniques in different enclosures. *J Nanofluids* 2022;11:155–168. [\[CrossRef\]](#)
- [7] Gul T, Usman M, Khan I, Nasir S, Saeed A, Khan A, Ishaq M. Magneto hydrodynamic and dissipated nanofluid flow over an unsteady turning disk. *Adv Mech Eng* 2021;13:1–11. [\[CrossRef\]](#)
- [8] Mahdy A, Chamkha AJ. Unsteady MHD boundary layer flow of tangent hyperbolic two-phase nanofluid of moving stretched porous wedge. *Int J Numerical Methods Heat Fluid Flow* 2018; 28:2567–2580. [\[CrossRef\]](#)
- [9] Abderrahmane A, Qasem NAA, Younis O, Marzouki R, Mourad A, Shah N A, Chung J D. MHD hybrid nanofluid mixed convection heat transfer and entropy generation in a 3-D triangular porous cavity with zigzag wall and rotating cylinder. *Math* 2022;10:769. [\[CrossRef\]](#)
- [10] Islam T, Yavuz M, Parveen N, Fayz-Al-Asad Md, Impact of non-uniform periodic magnetic field on unsteady natural convection flow of nanofluids in a square enclosure. *Fractal Fract* 2022;6:101. [\[CrossRef\]](#)
- [11] Vaidya H, Rajashekhar C, Mebarek-Oudina F, Prasad KV, Vajravelu K, Ramesh BB. Examination of chemical reaction on three-dimensional mixed convective magnetohydrodynamic Jeffrey nanofluid over a stretching sheet. *J Nanofluids* 2022;11:113–124. [\[CrossRef\]](#)
- [12] Abbas Z, Hussain S, Naveed M, Nadeem A, Ali A. Analysis of joule heating and generalized slip flow in ferromagnetic nanoparticles in a curved channel using Cattaneo- Christof heat flux theory. *Therm Sci* 2022; 26: 437–448. [\[CrossRef\]](#)
- [13] Jilte R, Mohammad HA, Ravinder K, Vilas K, Amirhosein M. Cooling Performance of a Novel Circulatory Flow Concentric Multi-Channel Heat Sink with Nanofluids. *Nanomaterials* 2020;10:647. [\[CrossRef\]](#)
- [14] Jilte R, Ravindra K, Mohammad HA. Cooling performance of nanofluid submerged vs. nanofluid circulated battery thermal management systems. *J Cleaner Prod* 2019;240:118131. [\[CrossRef\]](#)
- [15] Buongiorno J. Convective Transport in Nanofluids. *ASME J Heat Transf* 2006;128:241–250. [\[CrossRef\]](#)
- [16] Abdullah A, Ibrahim F, Chamkha A. Nonsimilar solution of unsteady mixed convection flow near the stagnation point of a heated vertical plate in a porous medium saturated with a nanofluid. *J Porous Media* 2018;21:363–388. [\[CrossRef\]](#)
- [17] Mabooda F, Mastroberardino A. Melting heat transfer on MHD convective flow of a nanofluid over a stretching sheet with viscous dissipation and second-order slip. *J Taiwan Int Chem Eng* 2015;57:62–68. [\[CrossRef\]](#)

- [18] Mahdy A, Chamkha AJ. Heat transfer and fluid flow of a non-Newtonian nanofluid over an unsteady contracting cylinder employing Buongiorno's model. *Int J Numerical Methods Heat Fluid Flow* 2015;25:703–723. [\[CrossRef\]](#)
- [19] Pavlov KB. The magnetohydrodynamic flow of an incompressible viscous fluid is caused by the deformation of a plane surface. *Magn Hidrodin* 1974;4:146–147.
- [20] Andersson H I. MHD flow of a viscoelastic fluid past a stretching surface. *Acta Mech* 1992;95:227–230. [\[CrossRef\]](#)
- [21] Kasiviswanathan SR, Gandhi MV. A class of exact solutions for the MHD flow of micropolar fluid. *Int J Eng Sci* 1992;30:409–417. [\[CrossRef\]](#)
- [22] Chamkha AJ, Rashad A M, Armaghani T, Mansour MA. Effects of partial slip on entropy generation and MHD combined convection in a lid-driven porous enclosure saturated with a Cu–water nanofluid. *J Therm Anal* 2018;132:1291–1306. [\[CrossRef\]](#)
- [23] Falkner VM, Skan SW. Some approximate Solutions of the boundary-layer equations. *Lond Edinb Dublin Philos Mag J Sci* 1931;12:865–896. [\[CrossRef\]](#)
- [24] Schlichting H, Gersten K. *Boundary-Layer Theory*, Springer: Berlin, Germany, 2016.
- [25] Falkner VM, Skan SW. Some approximate solutions of the boundary layer for flow past a stretching boundary. *SIAM J Appl Math* 1931;49:1350–1358.
- [26] Goyal KP, Kassoy DR. Heat and mass transfer in a saturated porous wedge with impermeable boundaries. *Int J Heat Mass Transf* 1979;22:1577–1585. [\[CrossRef\]](#)
- [27] Stewartson K. Further solutions of the Falkner-Skan equation. *Math Procs Cambridge Philos Soc* 1954;50:454–465. [\[CrossRef\]](#)
- [28] Riley, Weidman PD. Multiple solutions of the Falkner-Skan equation for flow past a stretching boundary. *SIAM J Appl Math* 1989;49:1350–1358. [\[CrossRef\]](#)
- [29] Dimian MF. Effect of the magnetic field on forced convection flows along a wedge with variable viscosity. *Mech Mech Eng* 2004;7:107–117.
- [30] Ishak A, Nazar R, Pop I. Falkner-Skan equation for flow past a moving wedge with suction or injection. *J Appl Math Comput* 2007;25:67–83. [\[CrossRef\]](#)
- [31] Fang T, Zhang J. An exact analytical solution of the Falkner-Skan equation with mass transfer and wall stretching. *Int J Non-Linear Mech* 2008;43:1000–1006. [\[CrossRef\]](#)
- [32] Dogonchi AS, Chamkha AJ, Seyyedi SM, Ganji D D. Radiative nanofluid flow and heat transfer between parallel disks with penetrable and stretchable walls considering Cattaneo–Christov heat flux model. *Heat Transfer—Asian Res* 2018;47:735–753. [\[CrossRef\]](#)
- [33] Zheng L, Zhang C, Zhang X, Zhang J. Flow and radiation heat transfer of a nanofluid over a stretching sheet with velocity slip and temperature jump in a porous medium. *J Franklin Inst* 2013;350:990–1007. [\[CrossRef\]](#)
- [34] Ahmed S E, Hussein A K, Mansour M A, Raizah Z AS, Zhang X. MHD mixed convection in trapezoidal enclosures filled with micropolar nanofluids. *Nanosci Tech: An Intl J* 2018;9:343–372. [\[CrossRef\]](#)
- [35] Bagh A, Khan S A, Hussein A K, Thumma T, Hessain S. Hybrid nanofluids: Significance of gravity modulation, heat source/ sink, and magnetohydrodynamic on dynamics of a micropolar fluid over an inclined surface via finite element simulation. *Appl Math Comp* 2022;419:126878. [\[CrossRef\]](#)
- [36] Kasmani R, Sivasankaran S, Bhuvanewari M, Hussein A K. Analytical and numerical study on convection of nanofluid past a moving wedge with Soret and Dufour effects. *Int J Numerical methods Heat fluid flow* 2017;27:2333–2354. [\[CrossRef\]](#)
- [37] Ashraf M, Rehman S, Farid S, Hussein AK, Ali B, Shah N, Weera W. Insight into the significance of bioconvection on MHD tangent hyperbolic nanofluid flow of irregular thickness across a slender elastic surface. *Math* 2022;10:2592–25608. [\[CrossRef\]](#)
- [38] Ahmed S, Hussein AK, Mohammed H, Sivasankaran S. Boundary layer flow and heat transfer due to permeable stretching tube in the presence of heat source/sink utilizing nanofluids. *Appl Math Comp* 2014;238:149–162. [\[CrossRef\]](#)
- [39] Sudarsana RP, Chamkha AJ. Soret and Dufour effects on MHD heat and mass transfer flow of a micropolar fluid with thermophoresis particle deposition. *J Naval Arch Marine Eng* 2016;13:1813–8235. [\[CrossRef\]](#)
- [40] Narender G, Govardhan K, Sarma S. Viscous dissipation and thermal radiation effects on the flow of maxwell nanofluid over a stretching surface. *J Nonlinear Anal Appl* 2021;12:1267–1287. [\[CrossRef\]](#)
- [41] Mishra SR, Khan I, Al-Dallal Q M, Asifa T, Free convective micropolar fluid flow and heat transfer over a shrinking sheet with a heat source. *Case studies Therm Eng* 2018;11:113–119. [\[CrossRef\]](#)
- [42] Stewartson K. Further solutions of the Falkner-Skan equation. *Math Proceedings Cambridge Philos Soc* 1954;50:454–65. [\[CrossRef\]](#)